FABRICATION AND PROPERTIES OF POLYPYRROLE NANOCYLINDERS

FABRICATION AND PROPERTIES

OF

POLYPYRROLE NANOCYLINDERS

By

JEFFREY M. MATIVETSKY, B.Sc.

A Thesis

Submitted to the School of Graduate Studies

in Partial Fulfillment of the Requirements

for the Degree

Master of Science

McMaster University

MASTER OF SCIENCE (2001) McMaster University

(Physics) Hamilton, Ontario

TITLE: Fabrication and Properties of Polypyrrole Nanocylinders

AUTHOR: Jeffrey M. Mativetsky, B.Sc. (McGill University)

SUPERVISOR: Professor W.R. Datars

NUMBER OF PAGES: xiv, 129

ABSTRACT

Polypyrrole nanocylinders were fabricated by chemically synthesizing polypyrrole within the pores of nanoporous polycarbonate particle track-etched membranes and alumina membranes. The morphology of the nanostructures was characterized by transmission electron microscopy and scanning electron microscopy. The polycarbonate membrane-templated nanocylinders were cigar-shaped, with the diameter at the center being up to 2.5 times the diameter at the ends. The nanostructures produced in alumina membranes were linear aggregates of blobs. The electrical conductivity of the nanocylinders was measured by leaving the nanocylinders embedded in the insulating template membrane and measuring the trans-membrane resistance. The smallest diameter polycarbonate membrane-templated nanocylinders exhibited a slightly lower conductivity relative to the larger diameter nanocylinders. The temperature dependence of the resistance with and without the application of a magnetic field was in accordance with Mott variable range hopping at temperatures above 5 ± 1 K and Efros-Shklovskii variable range hopping at temperatures below 5 ± 1 K. Based on the measurements in the Mott regime, the localization length, the density of states at the Fermi energy, and the temperature dependence of the average hopping distance were calculated.

ACKNOWLEDGEMENTS

I am grateful to the following people for their help: my supervisor, Professor W. R. Datars for his valuable advice; Paul Dube, Zac Buffet, P. K. Ummat, M. Barati, and J. C. L. Chow for teaching me some experimental techniques; Andy Duft for his AFM work and for lending me his "mini vice grip"; Fred Pearson for his TEM work; and Professor G. M. Luke for allowing me to use his Oxford measurement system.

TABLE OF CONTENTS

LIST OF FIGURES

LIST OF TABLES

CHAPTER 1

INTRODUCTION

In the regime which lies between molecular and bulk scales, materials can possess unique properties on account of their size. There is currently much excitement over the prospect of observing such size-effects in nanoscopic systems. Not only is it expected that the study of nanostructures will lead to new fundamental physical insights, but these nanoscopic materials hold a lot of promise for technological applications.

Template synthesis is an elegant approach to fabricating nanostructures. The method involves the synthesis of a desired material within the pores of a nanoporous membrane. This technique is quite general, and can be applied to the preparation of nanoscopic fibrils or tubules composed of metals, semiconductors, superconductors, and other materials (Martin, 1994). Nanocylinders[1] composed of polypyrrole, a conducting polymer, have been prepared by several groups (Martin, 1994; Duchet *et al.*, 1998; Demoustier-Champagne and Stavaux, 1999).

[1] The term nanocylinder is being used as a general term for nanofibril or nanotubule.

There are numerous reasons why polypyrrole is an interesting material to consider. Conducting polymers are a relatively new class of materials; hence, there is still much to be learned about their properties. Moreover, these polymers have enormous potential for use in technological applications such as solar cells, light-emitting diodes, batteries, and anti-static protective bags. Polypyrrole is superior to other conducting polymers because of its ease of preparation and its relative environmental stability.

In the present work, polypyrrole nanocylinders were fabricated by using the template-synthesis method. The morphology of the nanostructures was studied by transmission electron microscopy and scanning electron microscopy. In order to investigate the electrical properties of the nanocylinders, conductivity measurements were performed at temperatures ranging from room temperature to 1.8 K, with and without the application of a magnetic field.

CHAPTER 2

BACKGROUND

2.1 Conducting Polymers

2.1.1 General Remarks

All pure polymers are electrical insulators. Nevertheless, the conductivity of some polymers, termed conductive polymers, can be increased by many orders of magnitude upon doping with non-metallic agents. This was first demonstrated by Heeger, MacDiarmid, and Shirakawa, who were awarded the 2000 Nobel Prize in Chemistry for their efforts. In the early part of the 1970's, a researcher visiting Shirakawa accidentally used 1000 times more catalyst than usual while preparing polyacetylene. Although the resulting silvery film did not conduct electricity, it was thought that it may be possible to coax the metallic-looking material into conducting. The breakthrough came in 1977, when a ten million-fold increase in conductivity was observed following treatment of polyacetylene with iodine (Hjertberg *et al.*, 2001). At present, conducting polymers can be produced with room temperature conductivities ranging from about $10^{-12}\ \Omega^{-1}cm^{-1}$ to $10^{5}\ \Omega^{-1}cm^{-1}$ (Conwell, 1997).

The most important conducting polymers are shown in Figure 2.1. A structural characteristic common to all of these and other conducting polymers is the presence of an extended system of conjugated double bonds; that is, the presence of alternating single (σ) bonds and double (σ and π) bonds (Roth and Bleier,1987).

Polypyrrole
(PPy)

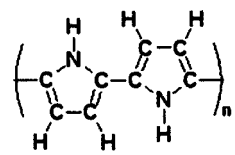

trans-Polyacetylene
(*t*-PA)

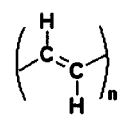

cis-Polyacetylene
(*c*-PA)

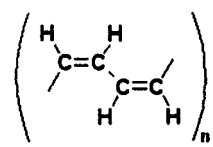

Polythiophene
(PT)

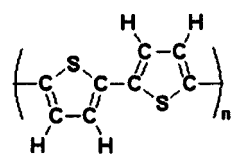

Poly(*p*-phenylene)
(PPP)

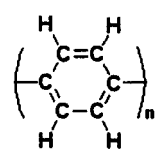

Poly(phenylenevinylene)
(PPV)

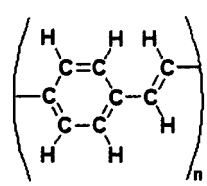

Figure 2.1 Chemical structure of polypyrrole and several other important conducting polymers.

2.1.2 Doping

The use of the term "doping" in the context of conducting polymers reflects the close analogy between the process of doping in conducting polymers and doping in conventional semiconductors: the introduction of an electron or hole within the host changes the host's electronic characteristics without significantly altering its overall structure.

Doping in conductive polymers is achieved by exposing the polymer to an oxidizing or reducing agent, the former results in p-type doping, and the latter results in n-type doping. The dopant becomes intercalated between polymer chains and there is a transfer of electrical charges between the dopant and the polymer (Roth and Bleier, 1987). This results in a conversion of the polymer from an insulating neutral polymer to an ionic complex which consists of a polymeric cation (or anion) and the reduced form of the oxidizing agent (or the oxidized form of the reducing agent) (Bredas and Street, 1985). Doping levels are usually in the range of 0.5-5% (Conwell, 1997).

2.1.3 Nature of Charge Carriers

A dopant ion either contributes an electron to a polymer chain or accepts an electron from a polymer chain. In polymers with a non-degenerate ground state, the addition of an electron or hole results in the creation of a bond

deformation pattern which extends over about 20 monomer sites (Conwell, 1997). Wherever the electron or hole migrates, the localized lattice distortion accompanies the charge. The electron and its associated deformation constitute what is called a *polaron.* The creation of a polaron also leads to a change in the energy level structure: An energy level, along with its two electrons, shifts from the valence band into the gap, and an empty level shifts from the conduction band into the gap. A positive polaron is formed by pulling an electron out of the lower gap level, while a negative polaron is formed by adding an electron to the higher gap level (Figure 2.2). Because one of the levels is half-filled, polarons have spin ½.

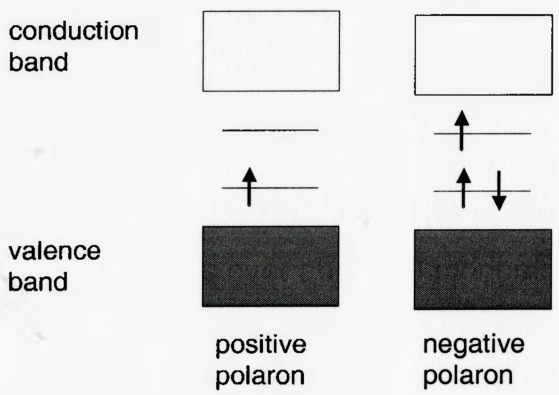

Figure 2.2 Schematic illustration of the energy level structure associated with positive and negative polarons.

If a second electron or hole is added, it may be added to the polaron or to another position on the polymer chain. In the former case, a *bipolaron* is created, while in the latter case, a second polaron is created. A bipolaron, which is defined as a bound state of two polarons of like charge, may be formed provided that the energy gained through a lattice distortion is greater than the Coulomb repulsion between the charges. In most conducting polymers, the creation of bipolarons is favored over the creation of two polarons (Bredas and Street, 1985). Like the polaron, the bipolaron is characterized by two energy levels in the gap. For the positive bipolaron, both of the levels are empty, while for the negative bipolaron, both of the levels are filled (Figure 2.3). The magnitude of the bipolaron's charge is twice that of an electron. Furthermore, because all of the states associated with the bipolaron are full (negative bipolaron) or empty (positive bipolaron), bipolarons are spinless.

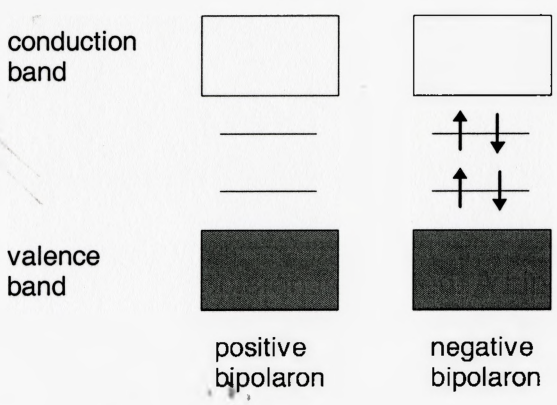

Figure 2.3 Schematic illustration of the energy level structure associated with positive and negative bipolarons.

A third type of charge carrier, called a *soliton*, occurs only in conducting polymers with a degenerate ground state. At present, *trans*-polyacetylene is the only known conducting polymer of this type. Much like a polaron, a soliton consists of a charge and an accompanying local lattice distortion. However, there is only one intra-gap energy level associated with a soliton. The level is empty in the case of the positive soliton and filled in the case of the negative soliton (Figure 2.4). Charged solitons have no spin.

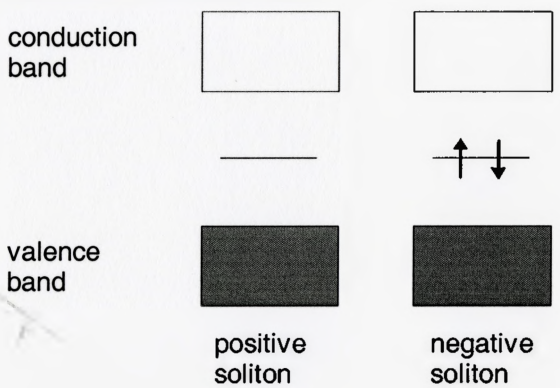

Figure 2.4 Schematic illustration of the energy level structure associated with positive and negative solitons.

Overall, the process of doping in conducting polymers generates localized states in the forbidden gap. Furthermore, in real samples, the presence of disorder, such as the random distribution of doping ions, the variant length of the polymer chains, and the presence of defects within a chain, results in a spreading of the conduction and valence bands. The states in the band tails are localized (Bottger and Bryksin, 1985).

2.2 Variable Range Hopping Conduction

2.2.1 Mott Variable Range Hopping

Phonon assisted tunneling, commonly referred to as *hopping*, is a mechanism for the transport of spatially localized charge carriers. It can be shown that the problem of calculating the dc hopping conductivity in a disordered medium in the presence of a weak electric field can be reduced to the problem of calculating the current in a random resistor network (Miller and Abrahams, 1960). The resistance between two lattice sites is inversely proportional to the corresponding hopping probability (Bottger and Bryksin, 1985).

At sufficiently high temperatures, there is a large probability that a charge carrier can couple to a phonon which has enough energy to facilitate a jump to a nearest neighbor. Consequently, nearest neighbor hops dominate at high temperatures and the temperature dependence T of the resistivity ρ can be written as

$$\rho = \rho_3 \exp\left(\frac{\varepsilon}{kT}\right) \tag{2.1}$$

where ρ_3 is a constant with units of resistivity, k is the Boltzmann constant, and ε is an activation energy.

At low temperatures, only the energy levels near the Fermi level are accessible. As a result, a charge carrier will preferentially hop to a remote site provided that this process requires less energy than a hop to a nearer site. This type of hopping is referred to as *variable range hopping*, because as the temperature is lowered, the hopping distance increases. Making use of the supposition that the density of states $N(E)$ is constant over the range kT at the Fermi energy E_F yields Mott's famous equation for variable range hopping in three dimensions (Mott and Davis, 1979), which reads

$$\rho = \rho_0 \exp\left[\left(\frac{T_0}{T}\right)^{1/4}\right] \tag{2.2}$$

where the characteristic temperature

$$T_0 = \frac{C_1}{kN(E_F)L_{loc}^3}. \tag{2.3}$$

Here L_{loc} is the localization length; that is, the distance over which a charge carrier's wavefunction decays to 1/e of its maximum value (Conwell, 1997). The

dimensionless constant C_1 has a value which lies in the range from 1.66 and 2.48, depending on the mathematical treatment used. It has been shown experimentally that there is a correlation between the characteristic temperature T_0 and the room temperature resistivity. In general, a larger value of T_0 corresponds to a larger room temperature resistivity. This can be understood by the fact that a large value of T_0, according to equation 2.3, implies a small density of states at the Fermi level and/or a highly localized charge carrier wavefunction.

The pre-exponential factor ρ_0 in equation 2.2 can have a weak temperature dependence, the exact form of which depends on the method used for its calculation. Most authors treat the pre-exponential factor as a constant. This is bolstered by the fact that experimentally, for films of amorphous semiconductors, excellent linearity has been observed in plots of $log(\rho)$ versus $T^{-1/4}$ (Mott and Davis, 1979). The deviations are so slight that the use of a particular temperature-dependent form for the pre-exponential factor cannot be justified.

The average hopping distance R_{hop} depends on temperature in the following manner:

$$R_{hop} = C_2\left(\frac{T_0}{T}\right)^{1/4} L_{loc} \tag{2.4}$$

where the dimensionless numerical constant C_2 has a value of about 3/8.

Generalizing to the case of arbitrary spatial dimension d, Mott's variable range hopping formula has the form (Shklovskii and Efros, 1984)

$$\rho = \rho_0^{(d)} \exp\left[\left(\frac{T_0^{(d)}}{T}\right)^{1/(1+d)}\right]. \tag{2.5}$$

The parameters $T_0^{(d)}$ and $\rho_0^{(d)}$ are the d-dimensional analogues of T_0 and ρ_0. Two-dimensional variable range hopping has been observed in thin films of amorphous germanium (Knotek *et al.*, 1973), silicon (Knotek, 1975), and carbon (Hauser, 1976). A transition from three to two-dimensional hopping took place when the thickness of the film was reduced to a size that was comparable to the calculated average hopping distance. The validity of the result for one-dimensional hopping is controversial. The difficulty arises from the fact that any large impedance, or blockade, which may be present in a one-dimensional chain,

cannot be bypassed and will dominate the temperature dependence. This results in a resistivity of the form

$$\rho \sim \exp\left[\frac{T_0'}{T}\right] \tag{2.6}$$

where T_0' is a constant. Nevertheless, calculations of the resistivity in quasi-one-dimensional systems consisting of many parallel chains of finite length lead to a relation of the same form as in equation (2.5) with $d = 1$ (Shante and Varma, 1973). It can be argued that this latter treatment is more relevant than the former for the consideration of actual samples.

2.2.2 Efros-Shklovskii Variable Range Hopping

Coulombic correlations between localized charge carriers can only be neglected if the correlation energies are much smaller than kT and other characteristic energies of the problem (Bottger and Bryksin, 1985). Shklovskii and Efros showed that the presence of long-range interactions between localized charge carriers leads to a parabolic dip in the density of states near the Fermi energy, a feature termed the *Coulomb gap* (Shklovskii and Efros, 1984). At the Fermi energy, the density of states vanishes. In this regime, variable range hopping takes the form

$$\rho = \rho_1 \exp\left[\left(\frac{T_1}{T}\right)^{1/2}\right] \tag{2.7}$$

where T_1 is the characteristic Efros-Shklovskii temperature and ρ_1 is a constant with units of resistivity. Crossovers from Mott variable range hopping to Efros-Shklovskii variable range hopping have been observed in inorganic semiconductors (Zhang *et al.*, 1990) and conducting polymers (Ghosh *et al.*, 1998) at low temperatures.

2.2.3 Magnetoresistance

In the presence of a magnetic field, the overlap of the localized wavefunctions decreases, resulting in a large positive magnetoresistance (Shklovskii and Efros, 1984). For the case of a constant density of states and a weak magnetic field H, the magnetic field dependence of the resistivity $\rho(H)$ is of the form (Shklovkii and Efros, 1984)

$$\ln\frac{\rho(H)}{\rho(0)} = t\left(\frac{L_{loc}}{L_H}\right)^4\left(\frac{T_0}{T}\right)^y \tag{2.8}$$

with $t = 5/2016$, $y = 3/4$. The quantity

$$L_H = \left(\frac{\hbar c}{eH}\right)^{1/2} \tag{2.9}$$

is the magnetic length. Here $\hbar$ is Planck's constant, c is the speed of light, and e is the charge of the electron. For the case where a Coulomb gap is present, $t = 0.0015$, and $y = 3/2$ (Shklovskii and Efros, 1984).

2.2.4 Remarks on the Observation of Variable Range Hopping

Although observations of variable range hopping have been reported in a great many papers, according to Hill, much of the evidence is insufficient (Hill, 1976). The standard practice is to demonstrate linearity in a plot of $\ln(\rho)$ as a function of T^{-x}, where $x = 1/4$, $1/3$, or $1/2$. Typically, any value of x between 1/4 and 1/2 fits the data reasonably well (Roth, 1995), so it is difficult to distinguish between Efros-Shklovskii variable range hopping and one, two, and three-dimensional Mott variable range hopping. Furthermore, the above procedure implicitly assumes that Mott or Efros-Shklovski variable range hopping is obeyed; however, if the density of states is neither constant nor parabolic or if a different conduction process is taking place, the value of x may differ from 1/4, 1/3, or 1/2.

An analysis method developed independently by Hill (Hill, 1976) and Zabrodskii (Zabrodskii and Zinov'era, 1984) explicitly determines the value of *x*. The method makes use of the fact that most known laws which describe the variation of resistivity with temperature are special cases of the general expression

$$\rho = BT^{-m} \exp\left[\left(\frac{\tilde{T}_0}{T}\right)^x\right] \tag{2.10}$$

where B, m, x, and $\tilde{T}_0$ are constants. Now, instead of investigating the resistivity directly, one considers the temperature dependence of the reduced local activation energy

$$w \equiv \frac{1}{T}\frac{\partial \ln \rho}{\partial (1/T)} = -\frac{\partial \log \rho}{\partial \log T}. \tag{2.11}$$

For a resistivity of the form given in equation (2.10),

$$w = m + x\left(\frac{\tilde{T}_0}{T}\right)^x. \tag{2.12}$$

If the resistivity has an exponential dependence, the second term in (2.12) will be much larger than the first at low temperatures. Taking the logarithm of both sides in the low temperature limit, one obtains

$$\log w \approx \log\left(x\tilde{T}_0^{\,x}\right) - x\log T. \qquad (2.13)$$

Therefore, at sufficiently low temperatures, a plot of log w versus log T is expected to yield a straight line, and the exponent x will be given by the slope.

Using the above outlined approach, Hill and Zabrodskii analyzed a large proportion of the experimental data available to them. For amorphous semiconductors, the analysis yielded values of x ranging from 0.18 to 0.7. However, most of the values were grouped around $x = 0.25$, indicating agreement with Mott variable range hopping conduction (Hill, 1976). The value of x for doped crystalline semiconductors ranged from 0.25 to 0.7 and were grouped around 0.5 (Zabrodskii and Zinov'era, 1984). This has been taken as evidence for the presence of Coulombic electron-electron correlations in doped semiconductors. Ghosh *et al.* used Hill and Zabrodskii's method to demonstrate a transition at 10 K from Mott's variable range hopping to Efros-Shklovskii variable range hopping in polyaniline, a conducting polymer (Ghosh *et al.*, 1998). The validity of Hill and Zabroskii's method was further illustrated by Bottger who showed that when $x \neq$ 1/2, 1/3, or 1/4, the precise determination of x can yield a reduction of the fitting

errors by up to an order of magnitude when plotting $\ln(\rho)$ as a function of T^{-x} (Bottger and Bryksin, 1985).

A common criticism of reports on the observation of Mott's variable range hopping is that the temperatures at which the resistivity is being measured are too high to be consistent with the theory; the temperatures sometimes being as high as room temperature. This qualm has been refuted by Pollak *et al.* who showed that although energy states which are far from the Fermi level may be accessible at moderate temperatures, there is an enormous weighting which favors the contribution of sites near the Fermi level (Pollak *et al.*, 1973).

2.2.5 Hopping Transport in Non-Metallic Conducting Polymers

For moderate doping levels, conducting polymers are semiconducting; that is, the resistivity increases as temperature is lowered. In this regime, only theories based on hopping have been in agreement with experimental findings (Conwell, 1997). Mott variable range hopping is the most successful and extensively used theory for conduction in conducting polymers. Three dimensional Mott variable range hopping has been observed over a large temperature range (10 K to 300 K) in polypyrrole (Meikap *et al.*, 1993), polyaniline (Ghosh *et.al.*, 1998), and polyacetylene (Epstein *et al.*, 1983).

The conductivity and the value of the characteristic temperature T_0 (see equations 2.2 and 2.3) are highly dependent on the preparation method, the doping level (Maddison and Tansley, 1992) and the choice of dopant. These factors affect the polymer chain lengths and the number of structural features such as substitutions and cross-links which may disturb conjugation within a chain. Experiments have shown, through the intentional inclusion of varying amounts of conjugation-breaking defects in polyacetylene, that an increase in the average conjugation length results in an increase in the conductivity of the polymer (Roth, 1991). It has been postulated that the degree of charge carrier delocalization is directly related to the conjugation length. This explains the correlation between conjugation length and conductivity. Improved electrical conductivity may also result from enhanced chain ordering due to stretching (Hagiwara *et al.*, 1990) or crystallization.

Below about 5 K in polypyrrole (Meikap *et al.*, 1993) and 10 K in polyaniline (Ghosh *et.al.*, 1998), Efros-Shklovskii variable range hopping has been observed. It is likely that the transition temperature is dependent on the process used in preparing the samples.

A large positive magnetoresistance has been observed in polypyrrole (Abou-Elazab *et al.*, 1996) and polyaniline (Ghosh *et al.*, 1998). At temperatures below 5 K, the magnetoresistance in polypyrrole is in conformity with the behavior

expected of a system of localized states with a strong Coulomb interaction (equation 2.8 with $t = 0.0015$, $y = 3/2$).

2.3 Membranes Used for Template Synthesis

2.3.1 Particle Track-Etched Membranes

Particle track-etched membranes are made by bombarding a polymer film with high energy heavy ions and then chemically etching the resulting damage tracks into pores. The diameter of the pores depends on etching time. The track-etch method can be used to produce membranes with a random distribution of parallel, uniformly cylindrical pores with mean pore diameters ranging from 15 nm to tens of microns (Piraux, *et al.*, 1999). The properties of commercial membranes are less ideal. The pores in commercial membranes have a cigar-like shape and have poor alignment, with an angular distribution of $\pm 34^{\circ}$ (Demoustier-Champagne and Stavaux, 1999). Nevertheless, the commercial membranes are suitable for template synthesis; the only difficulty added to the study of the resulting nanostructures is that the morphology is more difficult to characterize.

2.3.2 Porous Alumina Membranes

The anodic oxidation of aluminum in acid electrolytes, such as sulfuric acid, oxalic acid, or phosphoric acid, forms a porous alumina film on the aluminum. The pore size can be controlled either by varying the voltage used during anodic oxidation (Shingubara *et al.*, 1997) or by increasing pore size via etching in sulfuric acid (Itaya, *et al.*, 1984). The aluminum substrate can be selectively removed in an HCl, $CuCl_2$ solution (Itaya *et al.*, 1984). The resulting membranes have parallel pores which are arranged in a quasi-hexagonal array. The mean pore size can range from 5 nm to hundreds of nanometers (Martin, 1994). The shape of the pores in commercial porous alumina membranes can vary within a single membrane, with some pores having a nearly hexagonal cross section and others having an oval cross section (Mansouri and Burford, 1994).

2.4 Template-Synthesized Polypyrrole Nanocylinders

2.4.1 Synthesis and Morphology

Synthesis of polypyrrole can be achieved either electrochemically or with the use of a chemical oxidizing agent via the oxidative polymerization of pyrrole. During the synthesis of polypyrrole within the pores of a polycarbonate track-etched membrane, the nascent polymer is preferentially deposited along the walls of the pores. It was hypothesized by Martin that the nucleation along the pore

walls is due to an attraction between polycationic polypyrrole, which forms during polymerization, and anionic sites on the polycarbonate pore walls, which are present as a result of the track-etching process (Martin, 1994). Furthermore, while pyrrole is soluble, the polycationic form of polypyrrole is insoluble. Hence, it is believed that there is a solvophobic interaction which draws the polycationic polymer towards the pore walls.

Following nucleation along the pore walls, subsequent growth of polypyrrole thickens the tubule wall. According to Parthasarathy and Martin, the thickness of the nanotubule walls is directly related to the polymerization time. Moreover, after sufficiently long polymerization times, the tubules close, forming nanofibrils (Parthasarathy and Martin, 1994). This contrasts the findings of Duchet *et al.* who observed that thin-walled tubules were formed regardless of the polymerization time used. Solid nanofibrils were only formed after several successive iterations of polymerization followed by rinsing with water (Duchet *et al.*, 1998). The chemical synthesis techniques used by the two groups were similar in that they involved the use of the commercially fabricated particle track-etched membrane as a separating wall between two compartments, where one compartment contained the monomer solution and the other contained the oxidizing agent. The geometry of the two-compartment cells used were somewhat different: Parthasarathy and Martin had the monomer cell above the oxidizing agent cell, with the membrane sitting horizontally between the cells, while Duchet

et al. had the two cells side-by-side with the membrane sitting vertically between the cells.

The morphology of the polypyrrole nanocylinders was characterized by Duchet *et al.* using a field-effect scanning electron microscope. The nanocylinders were found to be cigar-shaped, with the middle portion having a diameter up to two times larger than the nominal pore diameter. The diameter at the nanocylinder ends was comparable to the nominal membrane pore diameter. Striations running perpendicular to the nanocylinder axis covered the surfaces of the nanocylinders. The patterning of the surface was attributed to the existence of crystalline domains along the polycarbonate membrane walls. During the fabrication of the membranes, the crystalline areas are etched at a lower rate than the amorphous ones, leaving striations along the pore walls (Duchet *et al.*, 1998).

Electrochemical synthesis of polypyrrole nanotubules was performed by Demoustier-Champagne and Stavaux (Demoustier-Champagne and Stavaux, 1999). The thickness of the tubule wall was dependent on the template membrane's pore diameter and on the choice of electrolyte. Homemade polycarbonate track-etched membranes were used as templates because of the improved regularity of their pore shape relative to commercially fabricated

membranes. Template synthesis within the homemade membrane pores yielded uniformly cylindrical nanocylinders.

2.4.2 Electrical Conductivity

Measurements of the room temperature electrical conductivity of polypyrrole nanocylinders (fibrils and tubules) have been performed by leaving the conducting nanocylinders within the pores of the insulating template membrane and measuring the resistance across the filled membrane (Cai *et al.*, 1991; Duchet *et al.*, 1998; Demoustier-Champagne and Stavaux, 1999). Provided that the electrical contact area A, the pore density n, the pore radius r and the membrane thickness L are known, the resistivity ρ can be calculated from the trans-membrane resistance R. For solid fibrils,

$$\rho = \frac{\pi r^2 nAR}{L}. \tag{2.14}$$

For hollow tubules,

$$\rho = \frac{\pi\left(r_o - r_i\right)^2 nAR}{L} \tag{2.15}$$

where r_o is the outside radius and r_i is the inside radius of the tubule. The conductivity is the inverse of the resistivity. To measure the resistance across a filled template membrane, Cai *et al.* used a pressure-contact. An applied pressure of 7×10^3 psi was required in order to obtain reproducible resistance data. In order to avoid the possibility of damaging the nanocylinders with the use of a high pressure, Duchet *et al.* and Demoustier-Champagne and Stavaux used silver paste and copper wires to contact the membranes.

During synthesis, in addition to the growth of polypyrrole within the pores of the template membrane, layers of polypyrrole grow on the membrane surfaces. These surface layers were left intact because they ensured contact between the polypyrrole nanocylinders and the electrical contacts. Cai *et al.* showed that the contribution of the surface layers to the trans-membrane resistance was less than 1% at room temperature (Cai *et al.*, 1991). This was achieved by using a four point method to measure the resistance $R_{||}$ along a surface layer. The resistivity is given by

$$\rho_S = \frac{R_{||} t w}{\ell} \tag{2.16}$$

where t is the thickness of the surface layer, w is the width of the voltage contacts, and ℓ is the length of the separation between the contacts. Assuming

that the resistivity of the surface layer is isotropic, the trans-surface resistance $R_{\perp}$ is

$$R_{\perp} = \frac{\rho t}{A} \tag{2.17}$$

where A is the area of the electrical contact used for a trans-membrane measurement.

The electrical conductivity of large-diameter polypyrrole nanocylinders (600 nm) was found by Cai *et al.* to be comparable to that of bulk polypyrrole samples. Smaller diameter nanocylinders were observed to have higher conductivities, with the conductivity of the smallest diameter nanocylinder, nominally 30 nm, being over an order of magnitude higher than that of bulk samples (Cai *et al.*, 1991). Similar results were obtained by Duchet *et al.* (Duchet *et al.*, 1998) and Demoustier-Champagne and Stavaux (Demoustier Champagne and Stavaux, 1999). It must be noted, however, that measuring the conductivity of the nanocylinders is difficult and prone to error because of the need for an accurate determination of several nanoscopic geometrical quantities. In light of this point, a critical discussion of the conductivity measurements performed by Cai *et al.*, Duchet *et al.*, and Demoustier-Champagne and Stavaux is given in chapter 4.

Four point conductivity measurements were performed by Martin *et al.* on thin films composed of polypyrrole nanotubules (Martin, 1994; Spatz *et al.*, 1994; Lorenz *et al.*, 1995, Orgzall *et al.*, 1996; Mikat *et al.*, 1999). The films were prepared by synthesizing nanotubules within the pores of a polycarbonate membrane, dissolving the membrane, collecting the nanotubules on a filter, and compacting the nanotubules in a pellet press. The temperature-dependence of the films' resistance conformed to Mott's variable range hopping model. It was observed that films prepared from 400 nm diameter nanotubules exhibited three dimensional variable range hopping, while films prepared from 50 nm diameter nanotubules exhibited two dimensional variable range hopping (Spatz *et al.*, 1994). It was proposed that the two-dimensional hopping was a result of the average hopping distance exceeding the thickness of the tubule wall. It was estimated that the hopping distance at 4.2 K was between 100 nm and 500 nm. Later studies reported a three to one-dimensional crossover at low temperatures in films composed of 400 nm nanotubules (Lorenz *et al.*, 1995).

2.4.3 Evidence for Enhanced Molecular Order

It was hypothesized by Cai and Martin that the enhanced conductivity in small-diameter polypyrrole nanocylinders is due to alignment of the polymer chains (Cai and Martin, 1989). A technique called polarized infrared absorption spectroscopy (PIRAS) was used the investigate the chain orientation in polypyrrole nanocylinders (Cai *et al.*, 1991).The technique involves the use of two

orthogonally polarized infrared beams. If the absorption intensities of the two polarizations are the same, then the polymer chains have no preferred orientation, whereas if the absorption intensities differ, the polymer chains are aligned to some degree. The ratio of the absorption intensities, called the *dichroic ratio*, provides a measure of the chain alignment. PIRAS was used to measure the dichroic ratio as a function of polymerization time for polypyrrole nanocylinders. The results indicated that the polypyrrole which was deposited directly on to the pore wall was aligned perpendicular to the axis of the nanocylinder. At later times, the extent of the ordering was decreased. The interpretation of Cai *et al.* was that subsequently deposited layers of polypyrrole are less ordered than the layer contacting the pore wall.

Martin proposed that the ordering of polypyrrole along the pore walls is due to a templating effect of the underlying polycarbonate chains, with the polypyrrole chains lying in registry with aligned polycarbonate chains (Martin, 1995). Subsequently deposited layers are less subject to the ordering-influence of the pore walls. This suggests that thinner nanocylinders consist of a larger proportion of ordered polypyrrole than thicker nanocylinders (see Figure 2.5). As a result, according to Cai *et al.*, smaller diameter nanocylinders have enhanced conductivites because they contain a higher proportion of ordered polypyrrole in comparison with larger diameter nanocylinders and bulk samples.

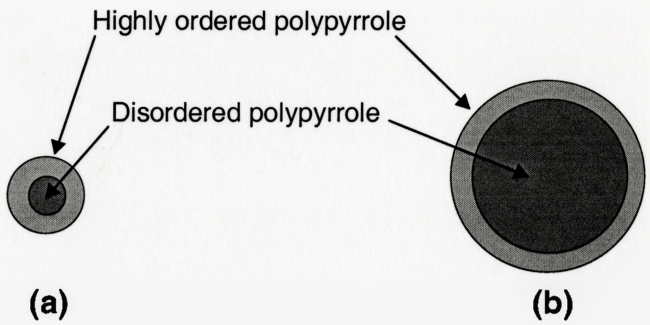

Figure 2.5 Cross-sectional view of the model proposed by Cai *et al.* for **(a)** small diameter and **(b)** large diameter template-synthesized nanofibrils.

In order to investigate the effect that chain alignment has on localization length in polypyrrole nanocylinders, Martin developed a method based on the theoretical work of Tian and Zerbi (Tian and Zerbi, 1990). According to Tian and Zerbi, the ratio of the absorption intensities of the 1560 cm^{-1} and 1480 cm^{-1} infrared bands, I_{1560}/I_{1480}, is inversely proportional to the localization length. Martin obtained corroborating evidence by showing that polymers with high concentrations of defects had high values of I_{1560}/I_{1480} and polymers with low concentrations of defects had low values of I_{1560}/I_{1480}. For template-synthesized polypyrrole nanocylinders, I_{1560}/I_{1480} was found to increase with polymerization time. Martin took this to suggest that the polypyrrole which coated the pore walls had extended conjugation and highly delocalized charge carrier states relative to the polypyrrole which was deposited afterwards (Martin, 1995).

It should be noted that the conductivity of chemically oxidized polypyrrole is affected by the polymerization time (Chen *et al.*, 1995). This consideration has not been taken into account by any of the groups studying polypyrrole nanocylinders. According to Chen *et al.*, the electrical conductivity of polypyrrole decreases when the polymerization time is increased. Doubling the reaction time nearly halves the electrical conductivity of the sample. It was proposed that the presence of the oxidation agent elicits irreversible degradation of the polymer's conjugated bonding system, resulting in a diminished conductivity. Thus, Martin's observed reduction in the localization length of the charge carriers in polypyrrole nanocylinders with increasing reaction time may be due to the degradation of the polymer, and not due to the addition of poorly conducting layers on to a more highly conducting layer.

CHAPTER 3

EXPERIMENTAL METHODS

3.1 Sample Preparation

3.1.1 Materials

Pyrrole (Alfa Aesar, 98%) was distilled immediately prior to use. Distillation was carried out with the glassware shown in Figure 3.1. The following procedure was employed: After freezing the pyrrole contained in the left arm in liquid nitrogen, the upper left terminal was connected to a vacuum line until a pressure of 5 mTorr was attained. At this point, the vessel was sealed by closing the upper left stopcock. The left arm was then removed from the liquid nitrogen-filled dewar and the right arm was immersed in liquid nitrogen. As the frozen pyrrole in the left arm melted and warmed to room temperature, its vapor pressure increased. The pyrrole vapor condensed in the cooler right arm. The contaminants were less volatile and did not contribute significantly to the condensate. The starting material provided by Alfa Aesar was brown and opaque, while the final product of the distillation procedure was colorless and transparent.

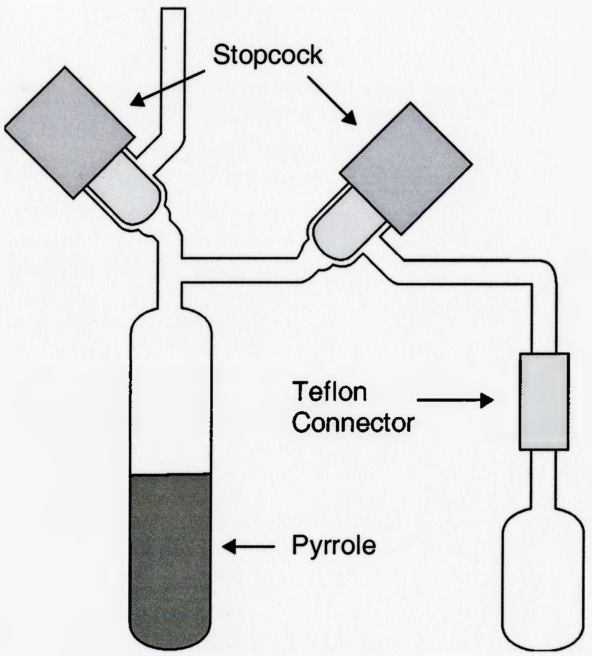

Figure 3.1 Schematic of the glassware used for the distillation of pyrrole.

Without distillation of the pyrrole, it was not possible to achieve adequate pore filling during the polymer synthesis. Filling in 50 nm and 100 nm pores was insufficient as indicated by the "infinite" trans-membrane resistance following polypyrrole synthesis. This was not the case when distilled pyrrole was used. Synthesis within 400 nm and 200 nm pores produced thin walled tubules when pyrrole was used as received (Figure 3.2 (a)). The degree of filling improved dramatically when distilled pyrrole was used (Figure 3.2 (b)). Moreover, it should be noted that the resistance of the nanocylinders produced from as-received pyrrole was about 1000 times higher than the resistance of those produced from distilled pyrrole.

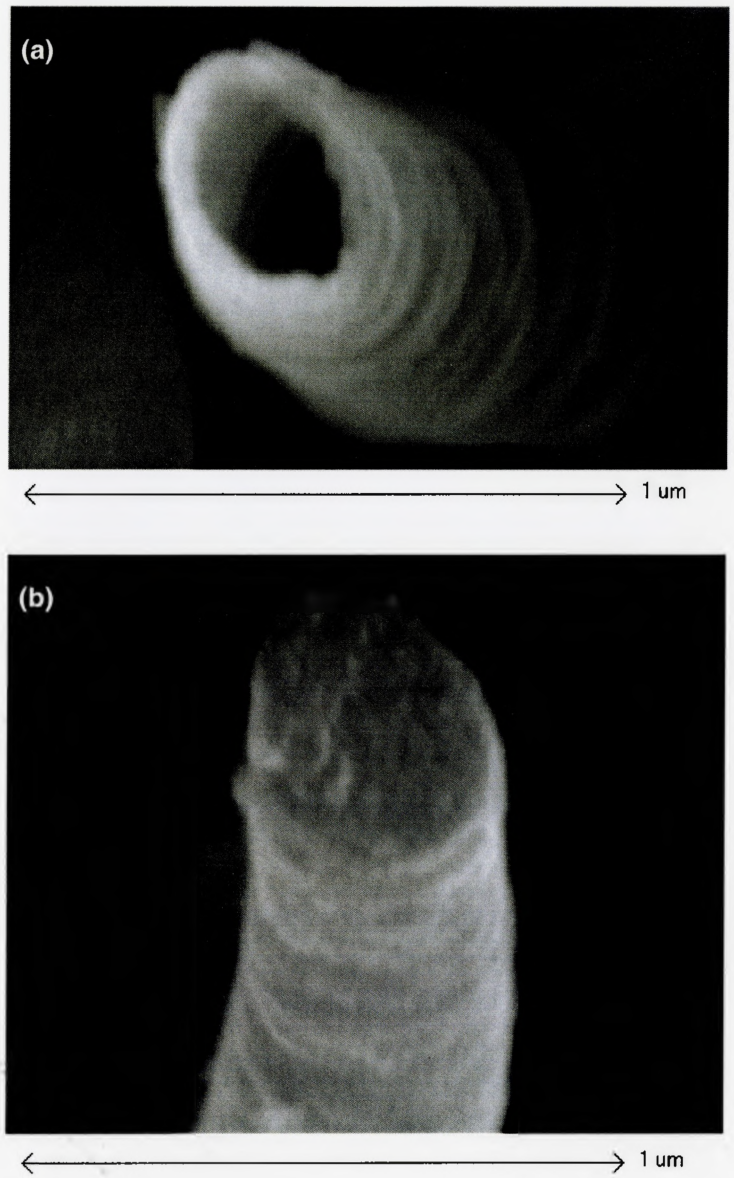

Figure 3.2 Scanning electron micrographs of polypyrrole nanocylinders synthesized in 400 nm polycarbonate membranes using **(a)** pyrrole that was not distilled, and **(b)** pyrrole that was distilled.

It was necessary to prepare the pyrrole immediately before use because it was noticed that with time (several weeks), the aqueous pyrrole solution gradually gained a dark green tint. This was probably due to the polymerization of pyrrole which may have resulted from interactions with air or light. The use of this aged distilled pyrrole yielded similar results to the case in which as-received pyrrole was used.

Deionized water was used to prepare aqueous solutions of pyrrole (0.5 M) and iron chloride (0.25 M, 0.5 M). The iron chloride solution was prepared from hydrated iron chloride lumps ($FeCl_3 \cdot 6H_2O$, Alfa Aesar 97-102%). The solution was filtered using filter paper.

Nuclepore® polycarbonate track-etched membranes and Anodisc™ alumina membranes, manufactured by Whatman, were used as templates for the synthesis of polypyrrole nanostructures. The membranes were circular and had a 25 mm diameter. Other specifications provided by Whatman are shown in Table 3.1. The rated pore density and pore diameter (at the surface) for the 100 nm polycarbonate membrane[1] were confirmed with the use of an atomic force microscope (AFM). Figure 3.3 shows an AFM image of a 100 nm Nuclepore® polycarbonate track etched membrane.

[1] The membranes will be identified by the pore diameters supplied by Whatman.

Table 3.1 Template membrane characteristics supplied by the manufacturer.

Membrane Type	Pore Diameter (nm)	Pore Density (pores/cm^2)	Thickness (μm)
Nuclepore® polycarbonate track-etched	50	$6x10^8$	6
	100	$3x10^8$	6
	200	$3x10^8$	10
	400	$1x10^8$	10
Anodisc™ alumina	20	N/A	60
	100	N/A	60

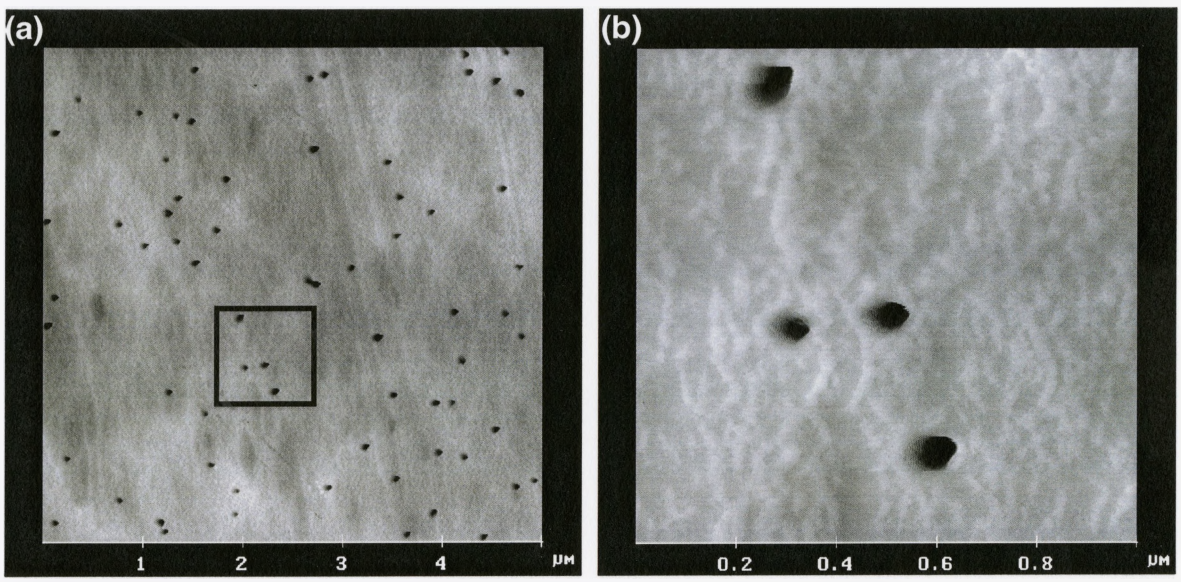

Figure 3.3 AFM images of a polycarbonate track etched membrane with a nominal pore diameter of 100 nm. An enlargement of the area outlined in **(a)** is shown in **(b)**.

3.1.2 Chemical Synthesis

For preliminary trials, the apparatus shown in Figure 3.4 was used for the chemical synthesis of polypyrrole nanocylinders. A procedure similar to that used by Duchet *et al.* was adopted (Duchet *et al.*, 1998). These experiments involved the use of polycarbonate membranes only. A template membrane was inserted between the two arms and was held in place by an O-ring on either side and a metal clip which gripped on to each arm's flange. Aqueous pyrrole (0.5 M) was added to the left compartment and was allowed to diffuse through the membrane for several minutes prior to the introduction of the oxidant reagent, iron chloride (0.5 M), into the right compartment. The reagents diffused through the pores of the membrane and reacted to yield polypyrrole nanostructures, which ran through the pores of the membrane, and thin polypyrrole films, which coated both surfaces of the membrane. The contrasting color of the white membrane and the black polypyrrole made it easy to observe whether polymerization had taken place. A reaction time of 30 minutes was used for 400 nm and 200 nm pores. Reaction times of up to 18 hours were required for significant filling in 100 nm and 50 nm pores. Following synthesis, the membranes were rinsed with copious amounts of deionized water, gently patted dry with filter paper, and dried overnight in an evacuated aluminum foil-covered desiccator. The samples were stored in an aluminum foil-covered desiccator, since it was observed that the conductivity of the samples gradually decreased after prolonged exposure to

humidity. Although it is not known whether the samples were light-sensitive, the aluminum foil ensured that the samples were protected from exposure to light.

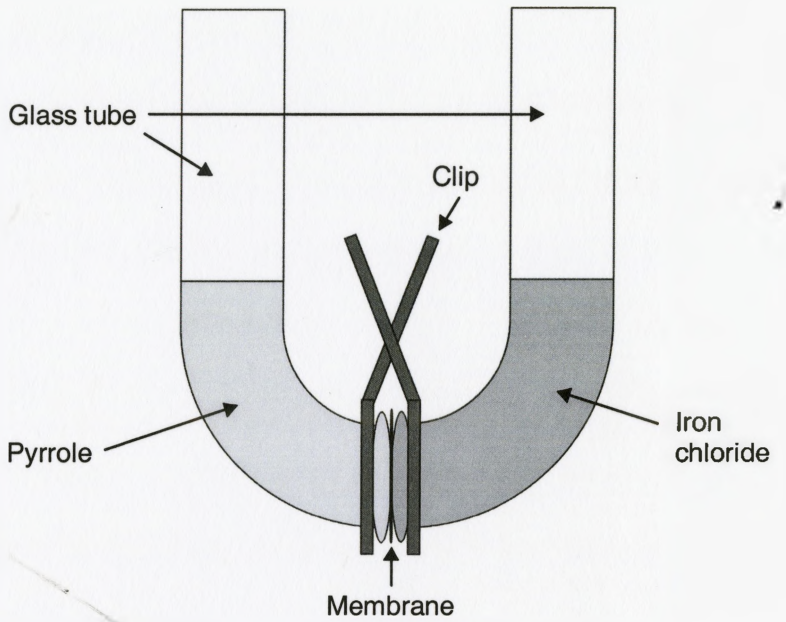

Figure 3.4 Schematic of the apparatus used for template-syntheses of polypyrrole nanocylinders during preliminary trials.

A problem encountered as a result of the procedure described above was the inhomogeneous filling of the template pores. More specifically, for 50 nm and 100 nm polycarbonate membranes, as illustrated in Figure 3.5 (a), only a crescent at the bottom end of the membrane was dark, indicating that only a small region of the membrane had polypyrrole-filled pores. A large portion of the

membrane remained unfilled even after reaction times exceeding 18 hours. This polymerization time is quite long relative to the 30 minutes used for synthesis within 200 nm and 400 nm pores. It was further noticed that between the black and white regions of the post-synthesis 50 nm and 100 nm templates, there was a darkness gradient. In 200 nm and 400 nm membranes, the surface layer was noticeably thicker at the bottom end. These observations suggest the possibility that even in the dark regions of the membranes, the pore filling may have been more complete in some parts than in others.

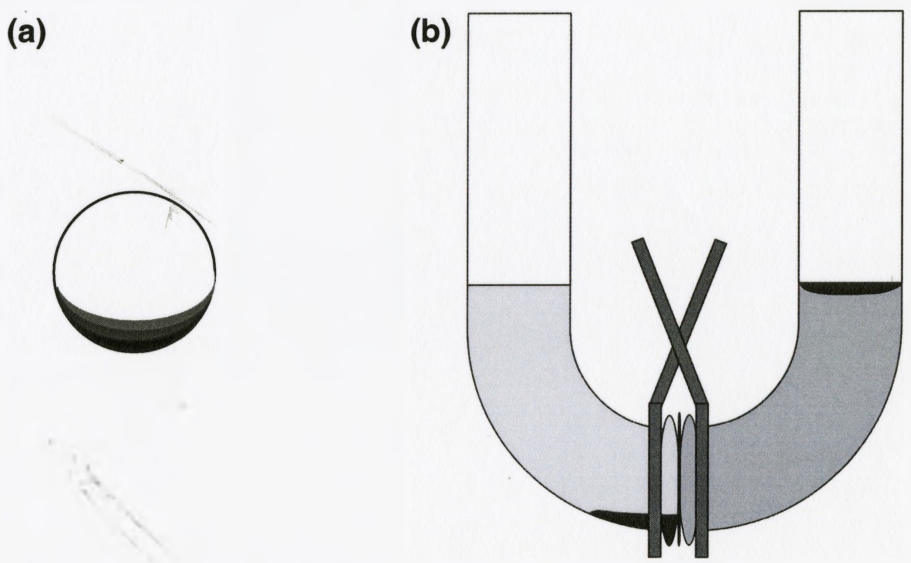

Figure 3.5 Schematic illustration of **(a)** the side view of a 50 nm or 100 nm template membrane following synthesis, **(b)** the accumulation of polypyrrole in the reaction vessel during synthesis. Dark regions represent polypyrrole.

The inhomogeneous pore filling appeared to be related to the location of excess polypyrrole during polymerization. As illustrated in Figure 3.5 (b), during synthesis, there was a visible accumulation of polypyrrole in two parts of the glassware: (1) In the compartment containing the pyrrole solution, polypyrrole collected at the bottom of the vessel, beside the bottom of the membrane. (2) In the iron chloride-containing compartment, polypyrrole floated to the top of the iron chloride solution. It is not understood exactly how gravimetric or solvophobic effects may have been responsible for the polypyrrole migration. Nevertheless, it appears likely that polypyrrole was preferentially formed in the pores at the bottom of the membrane because of the tendency for polypyrrole to be driven to that area, while filling in the top region of the membrane was poorer because of the tendency for polypyrrole to be driven away from that region.

The problem of inhomogeneous pore filling was remedied by adapting the reaction geometry. It was reasoned, based on the preceding observations, that by having the pyrrole compartment above the iron chloride compartment, with the membrane sitting horizontally between the compartments, the polypyrrole would tend to accumulate at the bottom of the top compartment and at the top of the bottom compartment; i.e. the polypyrrole would form in the vicinity of the membrane. Furthermore, since all parts of the membrane are at the same height, gravimetric and solvophobic effects would be the same for all parts of the membrane, and the polypyrrole growth would be isotropic across the surface of

the membrane. Indeed, this was the case. The reaction geometry was achieved in practice by using the apparatus shown in Figure 3.6. The long and short Nalgene tubes passed through and were gripped tightly by two separate holes in the rubber stopper. The rubber stopper was used to hold the long Nalgene tube in place, with one end in close proximity to the membrane. This tube allowed air which was trapped below the membrane to escape during iron chloride filling. The short tube provided an opening for the insertion of iron chloride.

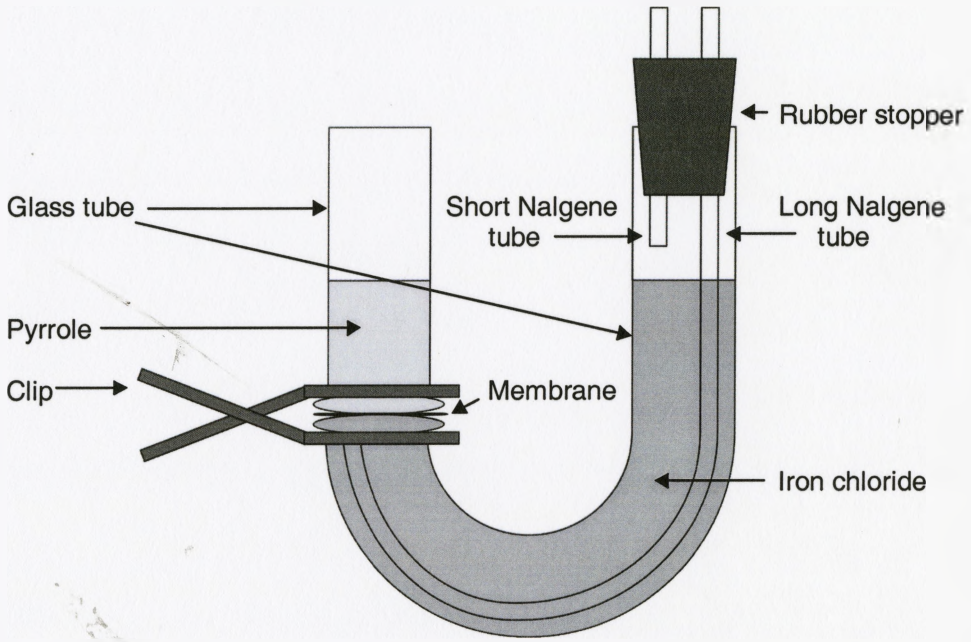

Figure 3.6 Diagram of the revised apparatus for the template-synthesis of polypyrrole nanocylinders.

Apparatus involving a horizontally-sitting membrane between pyrrole and iron chloride compartments was used by Cai (Cai *et al.*, 1991). Their set-up was not adopted for several reasons. In their implementation, heat-shrinkable Teflon

tubing was used to fasten the template membrane on to the end of a glass tube (Martin *et al.*, 1990). This way of mounting the membrane inevitably led to membrane stretching and distortion. Furthermore, the glass tube, with its attached membrane and protruding Teflon tubing, was placed standing, membrane-side down, in a beaker containing the iron chloride. This process probably trapped air bubbles below the membrane. It was observed in the present work that the presence of air bubbles during polymerization had an adverse affect on the conductivity of the sample.

Another point of concern arose from the discovery by Chen *et al.* who reported that the conductivity of chemically oxidized polypyrrole is affected by the polymerization time (Chen *et al.*, 1995). The optimal conditions, recommended by Chen *et al.*, for the chemical synthesis of polypyrrole are a reaction time of 30 minutes and a two-to-one pyrrole to iron chloride molar ratio.

Taking into account the considerations outlined above, the following refined procedure was used for the template synthesis of the polypyrrole nanocylinders. Sandwiched between two O-rings, a template membrane was clamped, using a metal clip, between the flanged ends of the straight and J-shaped glass tubes shown in Figure 3.6. The rubber stopper, with the long and short Nalgene tubes passing through its holes, was plugged into the open end of the J-shaped tube so that one end of the long tube was within a couple

millimeters of the membrane. Pyrrole solution (0.5 M), prepared from freshly distilled pyrrole, was pipetted into the straight glass tube (left side in Figure 3.6) until the solution's meniscus reached a height of about 3 cm above the membrane. The pyrrole solution was allowed to sit until a noticeable quantity of the solution diffused through the membrane. The times required for trans-membrane diffusion are given in Table 3.2. Once the pyrrole solution traversed the membrane, the iron chloride solution of optimal concentration (0.25 M) was pipetted through the short Nalgene tube into the J-shaped glass tube (right side in Figure 3.6) until the menisci of the two solutions were at the same level. It was important that the top of the solutions were at the same height; otherwise, the reaction would not have occurred at the membrane. This was made evident by the observation that if the iron chloride solution level was about a centimeter lower than the pyrrole solution level, polymerization occurred several millimeters below the membrane and the membrane remained unfilled.

Table 3.2 Trans-membrane diffusion times.

Membrane Type	Pore Diameter (nm)	Diffusion Time (minutes)
Nuclepore ® polycarbonate track-etched	50	25
	100	12
	200	3
	400	0
Anodisc™ alumina	20	90
	100	5

Two sets of experiments were performed. In the first set, 50 nm polycarbonate track-etched membranes were used as templates. Reaction times of 30, 60, and 120 minutes were employed in order to investigate whether pore filling improved as reaction time was increased. The second set of experiments involved the use of the same reaction time, 120 minutes, for all nanocylinder syntheses. This time was selected because transmission electron microscopy results, shown in Chapter 4, indicated that the 50 nm pores can be filled completely with the use of a 120 minute reaction time. Experience gained from early nanocylinder syntheses, using the side-by-side reaction geometry, suggested that 50 nm pores were more difficult to fill than larger diameter pores. Thus, based on the observation that 50 nm pores could be filled after a 120

minute reaction time, it was hoped that the larger diameter template membrane pores could also be completely filled after a 120 minute reaction time. That way, the only variable from sample to sample would be the nanofibril diameter. However, the morphology of the nanostructures resulting from the use of different diameter polycarbonate track-etched and aluminum oxide membranes turned out to be more complex than anticipated. These morphologies were characterized by transmission electron microscopy and scanning electron microscopy, and the results are presented in Chapter 4.

Following synthesis, copious amounts of deionized water were used to rinse the template membrane. The membrane was then gently patted dry with filter paper and placed in an evacuated aluminum foil-covered desiccator overnight for further drying. The samples were stored in an aluminum foil-covered desiccator.

3.2 Microscopy

3.2.1 Scanning Electron Microscopy

The surface structure of the polypyrrole nanocylinders was characterized with the use of a Philips 515 scanning electron microscope (SEM). Two types of measurements were performed. The first consisted of removing the layers of

polypyrrole which coated the membrane surfaces, dissolving the membrane, and observing the free nanocylinders. The second type of measurement involved breaking the filled template membrane and observing the membrane edge. This latter method allowed for the observation of a cross-sectional view of the surface layers as well as the observation of the nanocylinders embedded in the membrane.

The details of the sample preparation required for the observation of free nanocylinders are as follows: A piece of the filled template membrane, measuring about 1 cm^2 was placed on a flat surface. Scissors were used to cut the polycarbonate membrane-templated samples. Tweezers were used to break apart the brittle alumina membrane-templated samples. A few drops of a suspension of fine alumina powder in water were dripped on to the sample. Using gentle circular motion and a small amount of pressure, the flat bottom surface of a small beaker was used to agitate the alumina suspension which in turn polished the sample. After polishing each side of the membrane for several minutes, the sample was rinsed in water and ultrasonicated in water for 5 minutes in order to remove any remaining alumina powder. The samples were then patted dry with filter paper and dried for several hours in a desiccator. For nanocylinders synthesized within the pores of a polycarbonate membrane, the membrane was dissolved in dichloromethane and the freed nanostructures were caught on the surface of an alumina membrane. For nanocylinders synthesized within the pores

of an alumina membrane, the membrane was dissolved in sodium hydroxide and the freed nanostructures were caught on the surface of a polycarbonate membrane. The nanostructures were often connected by fragments of remaining surface layers and remained bundled together. The nanocylinder aggregates were scraped off the membrane with a sharp blade and held on to an SEM puck with silver paste.

The membrane-edge observations required minimal sample preparation. Two pairs of tweezers were used to cleanly break the membrane-nanocylinder composites. The polycarbonate-templated samples were flexible and had to be ripped apart while the alumina-templated samples were brittle and had to be fractured. Small pieces of the sample, measuring about 0.1 cm^2 in area, were held in the "mini vice grip" depicted in Figure 3.7, with the freshly broken edges facing upwards. The "mini vice grip" measured approximately a centimeter in diameter.

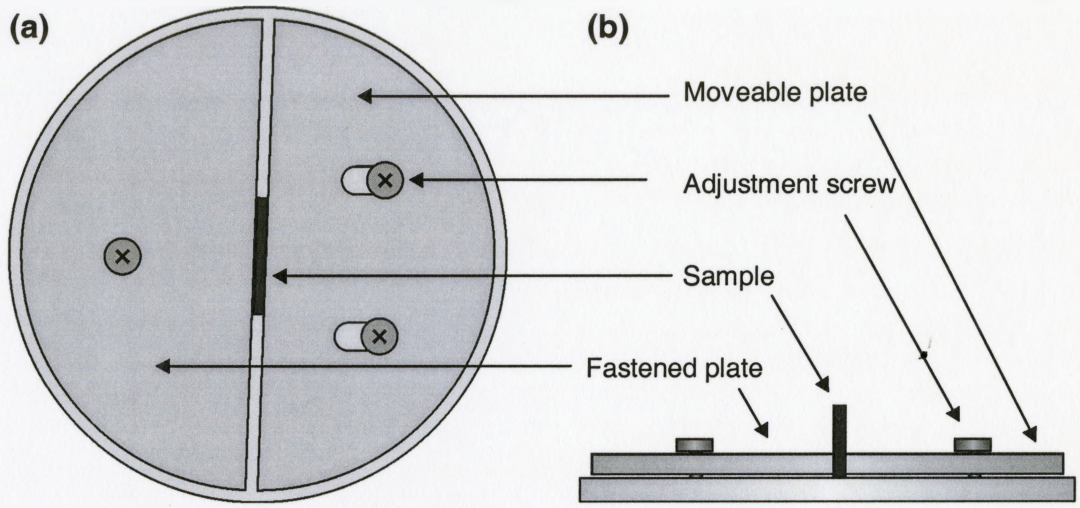

Figure 3.7 Diagram of the "mini vice grip" used for viewing the cross section of a filled template membrane: **(a)** top view, **(b)** side view.

Prior to observation under the SEM, an Edwards S150B sputter coater was used to deposit about 5 nm of gold on to the sample. The purpose of the gold layer was to eliminate surface charging effects. The sample space in the SEM was pumped to a base pressure of about 10^{-5} Torr. An accelerating voltage of 20 kV was employed for all observations.

3.2.2 Transmission Electron Microscopy

The internal structure of the polypyrrole nanocylinders was observed with the use of a Philips CM12 transmission electron microscope (TEM). The

microscopy was performed by Fred Pearson of the Brockhouse Institute for Materials Research.

The sample preparation for TEM observation was nearly the same as that for viewing freed nanocylinders under the SEM. However, rather than mounting the freed nanostructures on to an SEM puck, the nanostructures were placed in a small glass container which was partially filled with dichloromethane in the case of polycarbonate membrane-templated nanocylinders and deionized water in the case of alumina membrane-templated nanocylinders. The container was covered and swirled until the nanostructure aggregates broke apart into fine pieces. One drop of the resulting nanostructure suspension was dripped on to a TEM grid which consisted of a fine copper grid coated with a thin carbon film. The sample was ready for observation once all of the liquid on the grid evaporated. It should be noted that, for the case of alumina membrane-templated nanocylinders, it was necessary to rinse the nanostructures thoroughly with deionized water prior to their introduction into the glass container. This ensured that no remaining sodium hydroxide, which was used to dissolve the template, was present. Any residual sodium hydroxide would have left a coating on the nanostructures when the liquid was allowed to evaporate.

3.2.3 Atomic Force Microscopy

The surface of a 100 nm polycarbonate track-etched membrane was characterized with the use of a NanoScope II atomic force microscope (AFM). The microscopy was performed by Andy Duft of the Brockhouse Institute for Materials Research.

3.3 Resistivity and Magnetoresistance Measurements

3.3.1 Electrical Contacts

The resistance across the polypyrrole-filled template membranes was measured by using a two point method. A four point measurement across the sample was not possible because of the sample geometry. The procedure used for electrically contacting the samples is illustrated in Figure 3.8. A 44-gauge copper wire was attached with G. E. varnish to a 1 cm x 1 cm piece of a thin glass microscope cover slide. Silver paste was dabbed on to a small portion of the wire (Figure 3.8 (a)). Then, a sample measuring about 3 mm x 3 mm was positioned on top of the silver paste (Figure 3.8 (b)) and was gently pressed with a cotton swab. After placing a second 44-gauge wire on top of the sample and securing it to the cover slide with G. E. varnish, the wire was connected to the top of the sample with a dab of silver paste (Figure 3.8 (c)). This procedure was executed quickly in order to minimize the sample's exposure to humidity. The

contacted sample was placed in an aluminum foil-covered desiccator overnight in order to allow the silver paste to dry completely. Subsequently, the sample was coated with a solution of solid paraffin dissolved in liquid paraffin. The proportions used in preparing this paraffin solution were such that the solution's melting point was just above room temperature. That way, the sample could be coated with molten paraffin without subjecting it to elevated temperatures which may potentially cause damage. Once cooled to room temperature, the solid paraffin coating protected the sample from humidity. This minimized the sample's exposure to humidity while the sample's leads were being soldered to the resistivity probe head. It was verified that the paraffin coating did not affect the conductivity of a sample. As a further precautionary measure, the sample's conductivity was always measured soon after its synthesis in order to minimize possible aging effects.

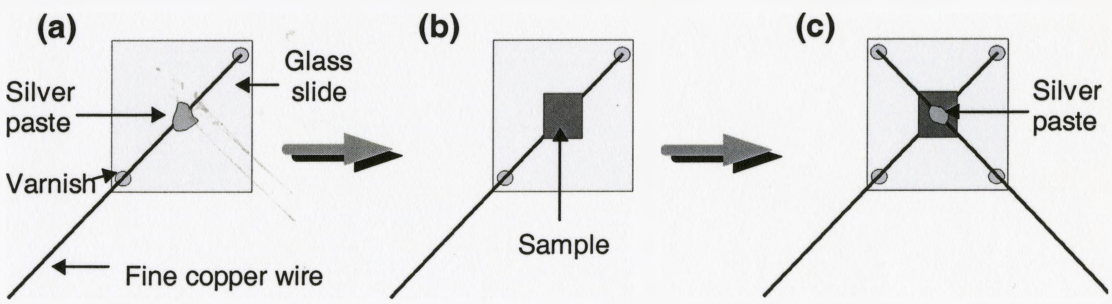

Figure 3.8 Sequence of steps for the preparation of a sample contact.

The areas of the silver paste contacts were carefully measured with the use of an Intel® QX3™ digital microscope. A digital image was taken of each side of the contacted samples. In the images, the silver paste had a very bright appearance, and the polypyrrole was nearly black. With the use of the Adobe Photoshop 5.0 graphics software, the images were made partially transparent by setting a parameter termed *opacity* to 50%. Then, the two images were superposed and aligned such that the sample edges and the wires overlapped perfectly (Figure 3.9 (a)). The brightest region of the composite image was where the two silver paste contacts overlapped. It is postulated that this is the effective area through which conduction takes place. The contrast of the composite image was adjusted until the brightest region was entirely white and the other areas were entirely black (Figure 3.9 (b)). The number of pixels in the region of interest was counted by Adobe Photoshop 5.0. A conversion from number of pixels to metric units of area was obtained from an image of a 0.2 mm grating, which was acquired by using the same level of magnification as for the sample images.

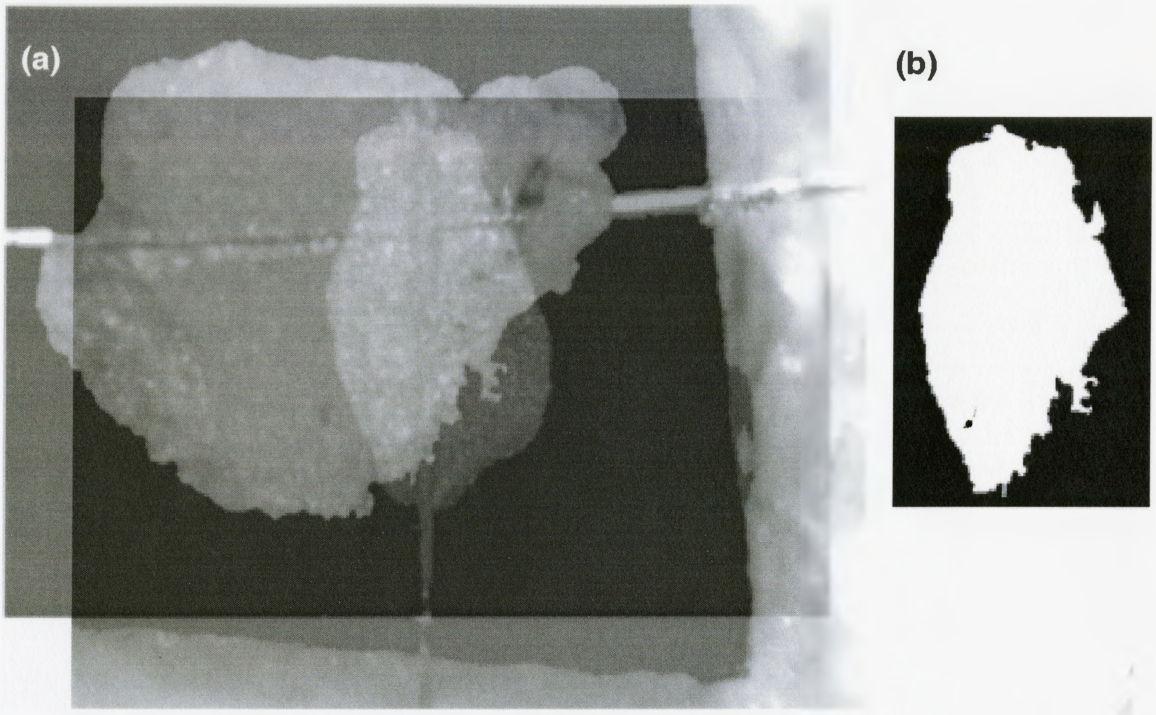

Figure 3.9 **(a)** Superposition of two aligned 50%-opaque silver paste contact images. **(b)** The overlap region becomes entirely white after increasing the contrast.

Out of concern that the solvent in the silver paste might affect the conductivity of the polypyrrole samples, the following test was used. Two samples were cut out from the same polypyrrole-filled template membrane. One sample was doused in butyl acetate, the solvent used in the GC Electronics silver paste, and then dried in an aluminum foil-covered desiccator. The second sample was used as a control. The resistance across the two samples was measured with a pressure-contact technique. Two microscope slides, each with gold contacts of

well defined area deposited on them, were used to sandwich a sample. A metal clip held the slides together with a constant pressure. These measures ensured that the two samples were subjected to the same measurement conditions; *i.e.*, the same contact area and the same applied pressure. A multimeter was used to measure the resistance between the opposing gold contacts. The two samples were found to have the same resistance, indicating that butyl acetate, and hence the silver paste, does not affect the conductivity of polypyrrole.

The polypyrrole surface layers were left intact for the trans-membrane resistance measurements. In order to ascertain that the surface layers' contribution to the resistance was negligible, a four point resistance measurement along the surface was performed. With the assumption that the resistivity was isotropic throughout the surface layer, it was possible to calculate the trans-surface resistance (see equations 2.16 and 2.17). This measurement was carried out at temperatures ranging from 300 K to 4.2 K. It was found that the contribution of the surface layers was less than 1% of the total trans-membrane resistance at all measured temperatures. The electrical contact scheme is shown in Figure 3.10. The two outermost contacts supplied the current. These were made to be longer than the contacts for measuring voltage so that the current density over the region where voltage was being measured was uniform. The uniformity was ensured by the absence of fringe effects at the centers of the current supplying contacts. The advantage of the four point measurement over

the two point measurement is that the current which flows through the voltmeter leads is much smaller than the current passing through the sample. Hence, the voltage drop across the voltage leads' contact resistances will be negligible in comparison with the voltage drop across the sample.

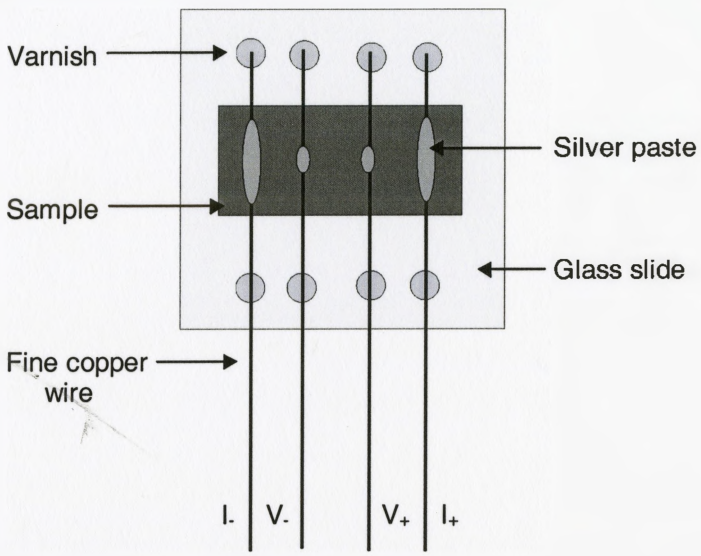

Figure 3.10 Four point contact scheme for measuring the resistivity along a polypyrrole surface layer.

3.3.2 Apparatus

Standard techniques were employed to measure the temperature dependence of the trans-membrane resistance with and without an applied magnetic field. A home-built apparatus was used to measure the sample resistance at temperatures ranging from 300 K to 4.2 K. Resistance and magnetoresistance measurements at temperatures ranging from 250 K to 1.8 K were performed by using an Oxford Instruments MagLab Exa™ multi-measurement system.

The resistivity probe head for the home-built apparatus, shown in Figure 3.11, consisted of a Kel-F sample platform, a carbon glass resistance (CGR) thermometer, a platinum thermometer, and four electrical terminals. The thermometers sat behind the sample, embedded in the Kel-F. They were coated with a thermally conducting compound so that they were in good thermal contact with the Kel-F. The CGR was used for measuring temperatures below about 77 K, while the platinum thermometer was used for measuring temperatures above about 77 K. Two of the electrical terminals were for supplying current to the sample. The two others were for measuring the voltage across the sample.

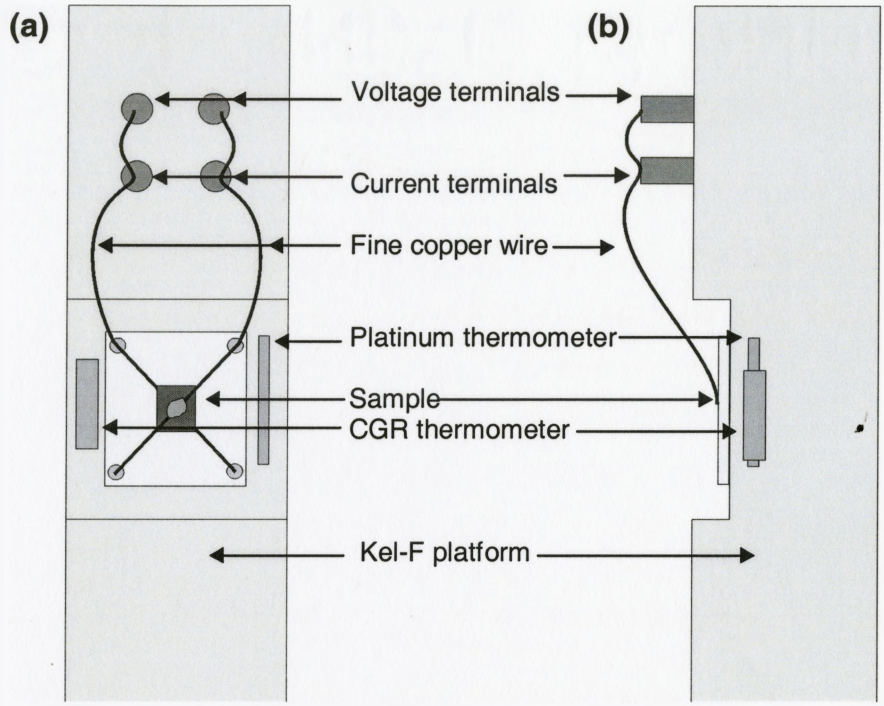

Figure 3.11 Schematic representation of the home-built resistivity probe head with a sample mounted: **(a)** front view, **(b)** side view.

The probe was placed in a dewar consisting of two compartments: (1) an inner cavity for the probe and either liquid helium or liquid nitrogen and (2) an outer liquid nitrogen jacket. The insulating dewar walls were evacuated with either a roughing pump or a diffusion pump.

A diagram of the electronic components used for measuring the temperature dependence of the resistance is shown in Figure 3.12. DC current was supplied to the sample by a Keithley 224 programmable current source. The

unit also transmitted the value of the current to the computer. A Keithley 2182 nanovoltmeter measured the voltage drop across the sample and forwarded the voltage reading to the computer. Home-built current sources supplied current to the thermometers. A Keithley 199 system DMM/scanner monitored the CGR current and sent the readings to the computer. It was unnecessary to perform similar measurements on the sample current or CGR current since the uncertainties associated with these quantities were less than 0.1%. A Keithley 705 scanner was used to switch between the two thermometer voltage signals and transmit them to the Hewlett Packard 3478A multimeter. The latter unit, in turn, measured the voltages and sent the readings to the computer. The data acquisition was computer-controlled. Approximately every 30 seconds, the current bias direction was switched. The absolute values of the forward and reverse bias voltage drops were averaged and used in conjunction with Ohm's law to calculate the sample resistance. Nearly every 60 seconds, the computer recorded the sample resistance and the thermometer temperatures.

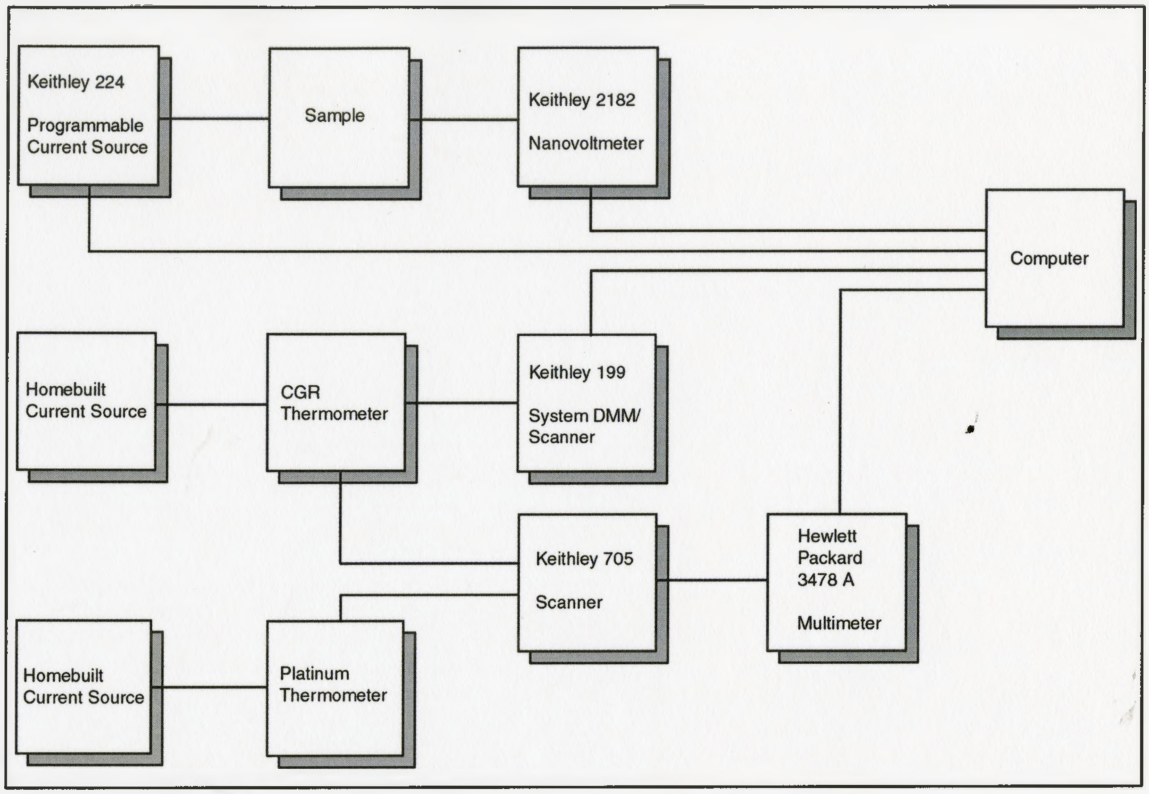

Figure 3.12 Block diagram of the interconnections between the components in the home-built resistivity apparatus.

The head of the Electrical Properties Rotation Probe for the Oxford measurement system is depicted in Figure 3.13. The sapphire plate acted as a stage for the sample. The thermometer was mounted on the underside of the sapphire plate, directly beneath the sample. There were two electrical terminals for supplying current and two for measuring voltage.

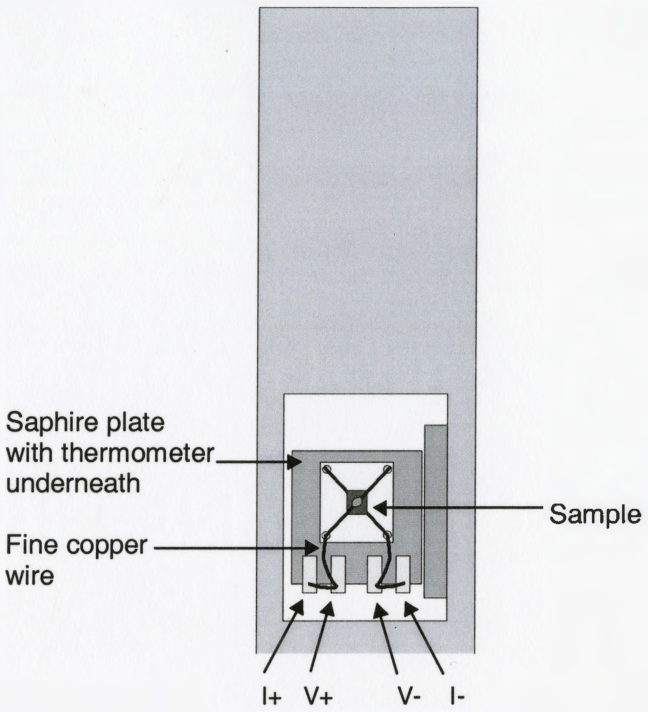

Figure 3.13 Schematic representation of the Oxford measurement system's resistivity probe head with a sample mounted.

The Oxford measuring system consisted of the basic units depicted in Figure 3.14. The system was computer-controlled; moreover, the MagLab measurement software enabled the user to specify the measurement conditions. Magnetic fields up to 9 T and temperatures down to 1.7 K were available. The superconducting magnet was oriented such that the applied field was transverse to the current direction. For temperature dependent measurements, the temperature was varied in steps. Typically 1 K steps were used for measurements above 10 K and 0.2 K steps were used for measurements below

10 K. The temperatures were set to the desired values by the ITC503 temperature controller, which adjusted the temperature until it was stabilized within a specified tolerance range. Once stability was achieved, the voltage across the sample was measured while using first a forward bias and then a reverse bias current. The absolute values of these two voltages were averaged.

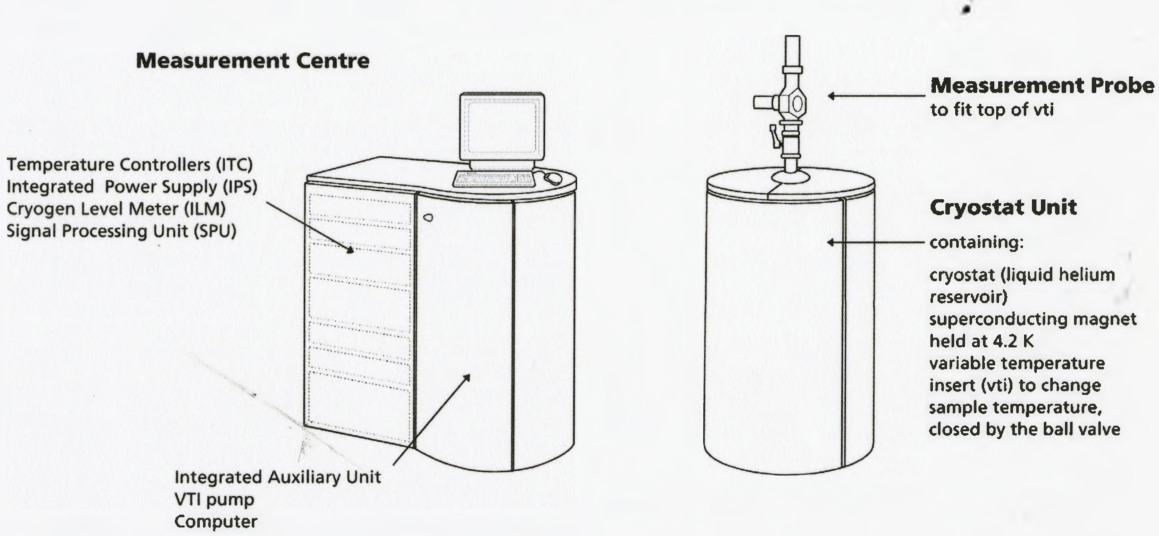

Figure 3.14 Schematic representation of the basic components of the Oxford Instruments MagLab Exa™ multi-measurement system (reproduced from manual).

3.3.3 Measurements

The procedure for performing measurements on the home-built apparatus will be described first. A small amount of vacuum grease was used to hold the sample's glass substrate on to the Kel-F platform of the resistivity probe

head. The sample leads were soldered to the probe's terminals. Although the measurement was a two point measurement, the voltage drop due to contact resistances was minimized by soldering the voltage contacts closer to the sample than the current contacts. Once the contacts were made, the probe head was wrapped with Teflon tape and a stainless steel cup was bolted over the end of the probe. These measures protected the sample from splashing liquid nitrogen or liquid helium. The probe was then lowered into the measurement station dewar, and the dewar was sealed. The sample space was evacuated and subsequently filled with helium gas. At this point, the outer dewar jacket was filled with liquid nitrogen and the data acquisition program was started.

For measurements down to 4.2 K, liquid helium was transferred to the inner compartment of the dewar once the sample temperature was below about 200 K. At times when it was unnecessary to attain such low temperatures, only liquid nitrogen was used as a cryogen. The sample cooling was sped up by inserting small amounts of liquid nitrogen into the inner compartment of the dewar. It was possible to maintain the sample temperature at 4.2 K or 77 K by filling the dewar with sufficient quantities of liquid helium or liquid nitrogen, respectively. Temperature dependent studies were performed while the system gradually warmed to room temperature. The warming rate was directly related to the quality of the vacuum in the dewar walls. Hence, the diffusion pump was used when very gradual warming was required (one and a half days to warm up), and

the roughing pump was used when a less gradual warming rate was desired (half a day to warm up).

For resistance and magnetoresistance measurements performed on the Oxford system, after mounting the sample's glass substrate on to the probe's sapphire platform with vacuum grease and soldering the sample leads to the probe's electrical terminals, the probe was lowered into the cryogenic dewar. The dewar was sealed, the sample space was evacuated and filled with low pressure helium gas. The computer interface was used to specify the measurement conditions.

In order to avoid non-Ohmic effects and sample heating, it was necessary to use sample currents as small as 10 - 1000 nA. Ohmic behavior was verified by measuring sample voltage as a function of current. It was sufficient to perform this measurement at the lowest temperature used because for all of the samples, the resistance increased with decreasing temperature; hence, the voltage across the samples was largest and the onset of nonlinear behavior was most pronounced at the lowest measured temperature. Sample heating was minimal since the power dissipated in the samples was never more than about 1 nW.

CHAPTER 4

RESULTS AND DISCUSSION

4.1 Nanostructure morphology

4.1.1 Effect of Polymerization Time

The reaction time used for the chemical synthesis of polypyrrole within the pores of a 50 nm polycarbonate membrane was varied in order to investigate whether the reaction time has an effect on the degree of pore filling. Three polymerization times were used: 30 minutes, 60 minutes, and 120 minutes. Analysis of the resulting nanostructures by transmission electron microscopy shows that the polypyrrole growth nucleates along the pore walls. As time progresses, the polymer continues to grow radially inwards from the pore walls. This is shown in Figure 4.1. After a reaction time of 30 minutes, hollow tubes are obtained (Figure 4.1 (a)). Subsequent growth thickens the tubule wall (Figure 4.1 (b)), until finally, after a reaction time of 120 minutes, the tubules close-up to form solid fibrils (Figure 4.1 (c)). The diameter of the hollow portion of the nanocylinders for the various polymerization times is given in Table 4.1.

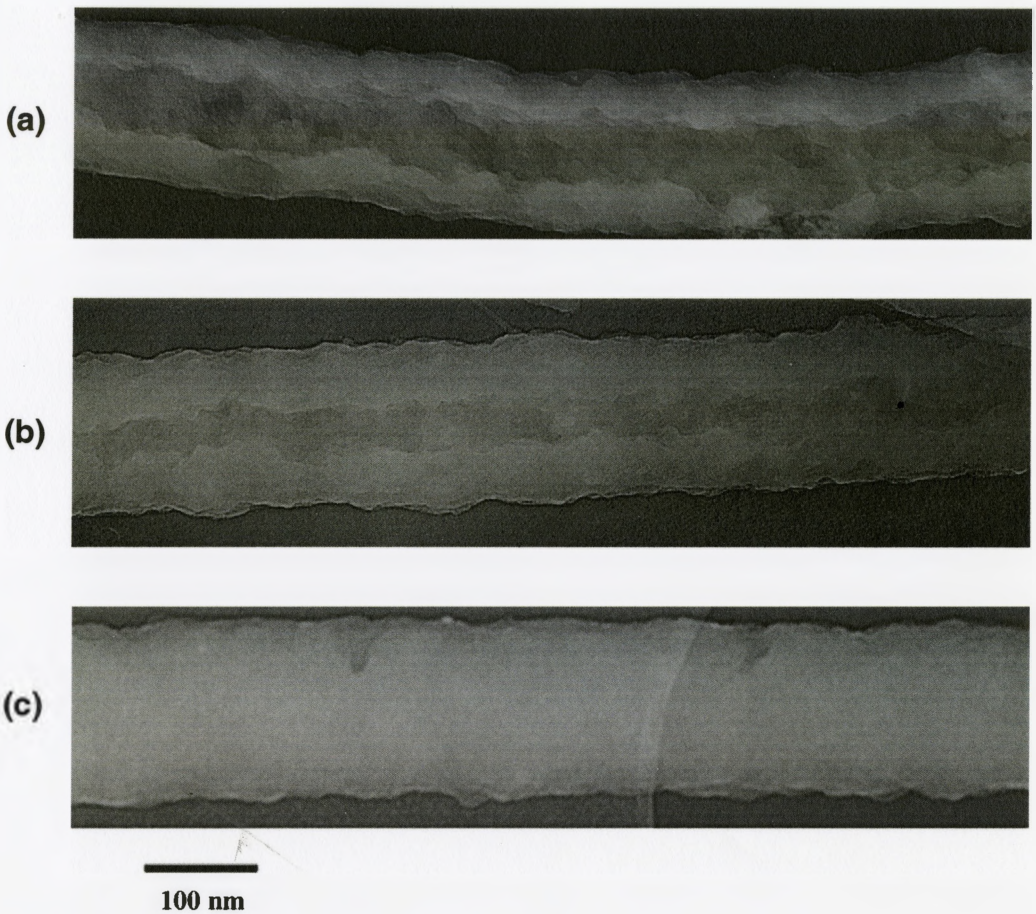

Figure 4.1 Transmission electron micrographs of 50 nm nanocylinders formed after polymerization times of **(a)** 30 minutes, **(b)** 60 minutes and **(c)** 120 minutes.

Table 4.1 Diameter of the tubule hollow for the three investigated reaction times.

Reaction Time (minutes)	Diameter of Tubule Hollow (nm)
30	70±10
60	40±10
120	0

As a result of the cigar-shaped pore profile in commercially fabricated polycarbonate membranes, the extremities of the polypyrrole nanostructures are tapered. It was observed for all of the reaction times investigated that the nanocylinder ends are fibrillar in nature (Figure 4.2). The length of the solidly filled region increases with reaction time. It is likely that at the extremities, where the pore diameters are smaller, the pores become completely filled sooner because there, the volume to be filled is small relative to the volume to be filled at other parts of the pore. Interestingly, as evidenced by the formation of entirely solid fibrils (Figure 4.1 (c)), the corking of the pores does not prevent further growth.

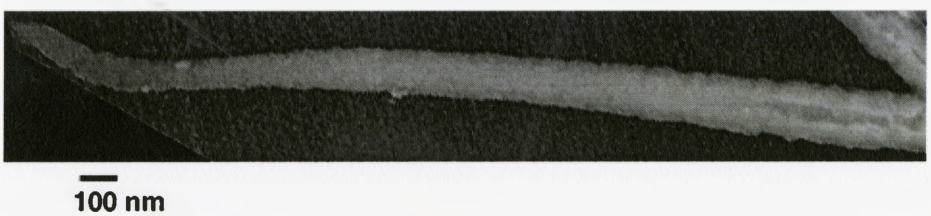

Figure 4.2 Transmission electron micrograph of the end of a polypyrrole nanocylinder, formed after a 60 minute polymerization time in a 50 nm polycarbonate membrane.

The above results are consistent with the report by Parthasarathy and Martin (Parthasarathy and Martin, 1994) that longer reaction times result in increased pore filling, and that after a sufficiently long polymerization time, the

pores fill completely. Duchet *et al.*, after observing that solid fibrils could not be formed without using several successive syntheses, conjectured that the tubule walls stopped thickening because the pores were blocked by the surface layer, which impeded the diffusion of the reagents within the pores (Duchet *et al.*, 1998). However, based on the above evidence that tubule wall thickening evolves despite blocking at the ends, this explanation appears to be incorrect. It is more probable that the incomplete filling observed by Duchet *et al.* may be a result of their use of a side-by-side reaction geometry. The problems associated with this geometry are cited in section 3.1.2.

4.1.2 Polycarbonate Membrane-Templated Polypyrrole Nanocylinders

Scanning electron micrographs of freed polycarbonate membrane-templated polypyrrole nanocylinders, synthesized using a 120 minute reaction time, are shown in Figures 4.3 - 4.5. Figure 4.3 shows a panoramic view of a typical free nanocylinder preparation. For the most part, the nanocylinders stand upright. However, in sections, the nanocylinders tip over and lie at an angle. Patches of vestigial surface layers are visible in some areas. Higher magnification views of leaning and upright nanocylinders are shown in Figures 4.4 and 4.5 respectively.

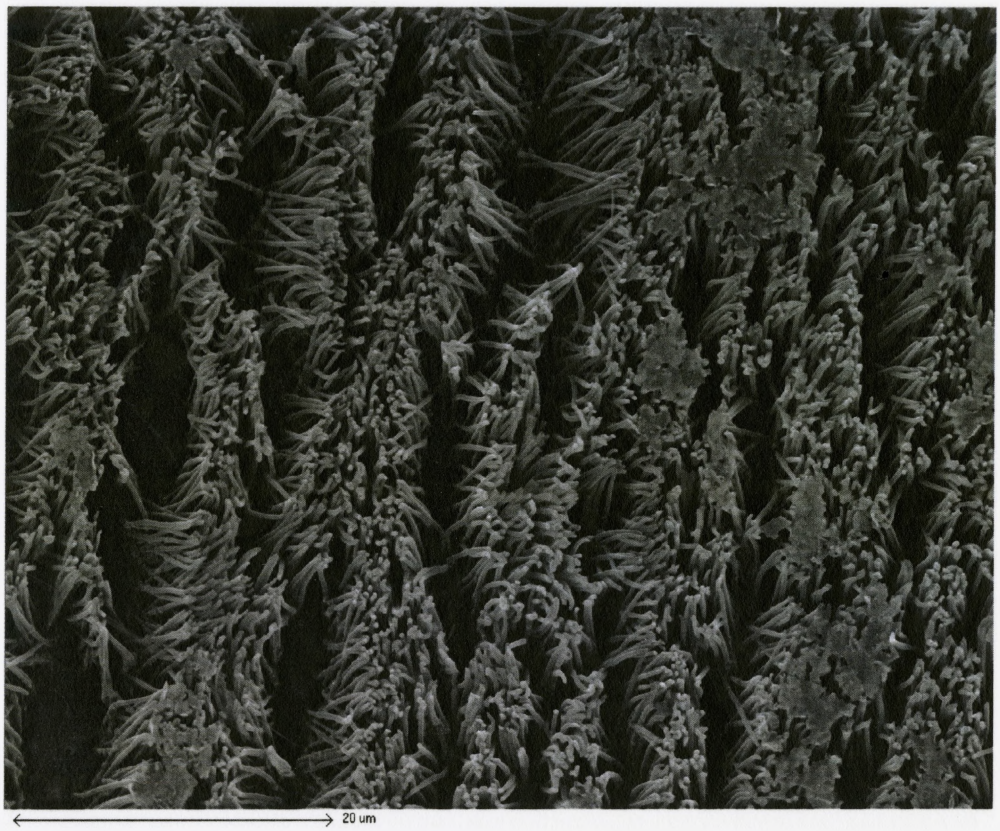

Figure 4.3 Scanning electron micrograph of free nanocylinders which were template-synthesized within the pores of a 200 nm polycarbonate membrane.

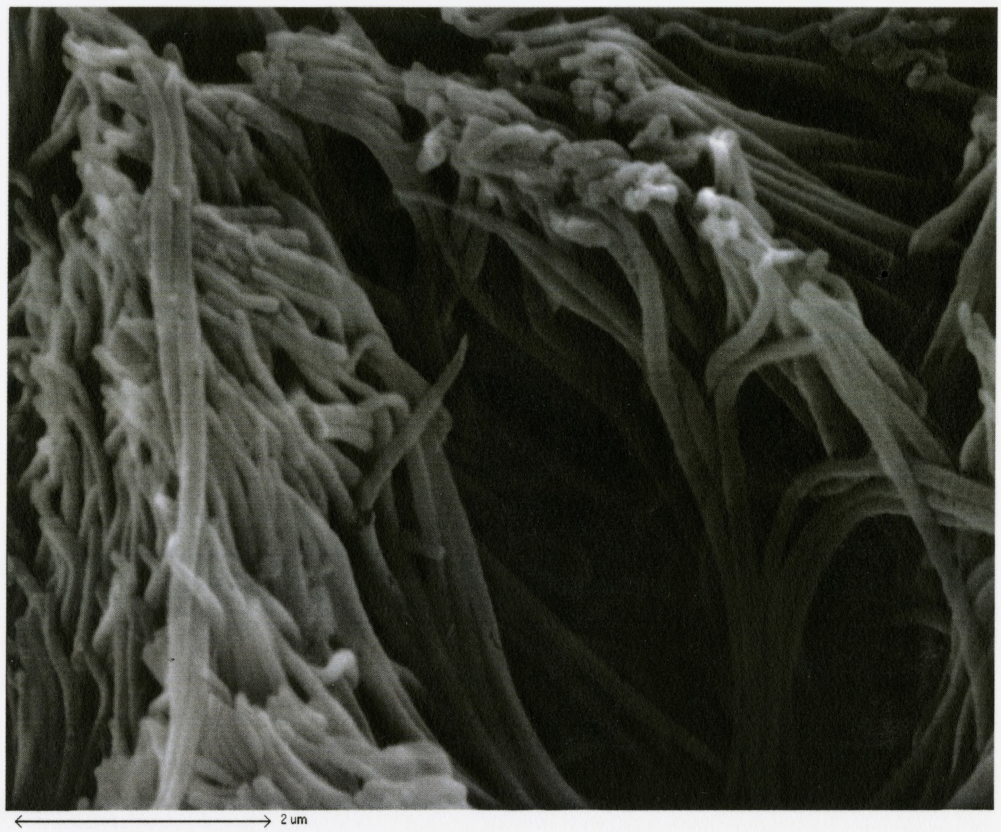

Figure 4.4 Scanning electron micrograph of leaning free nanocylinders which were template-synthesized within the pores of a 50 nm polycarbonate membrane.

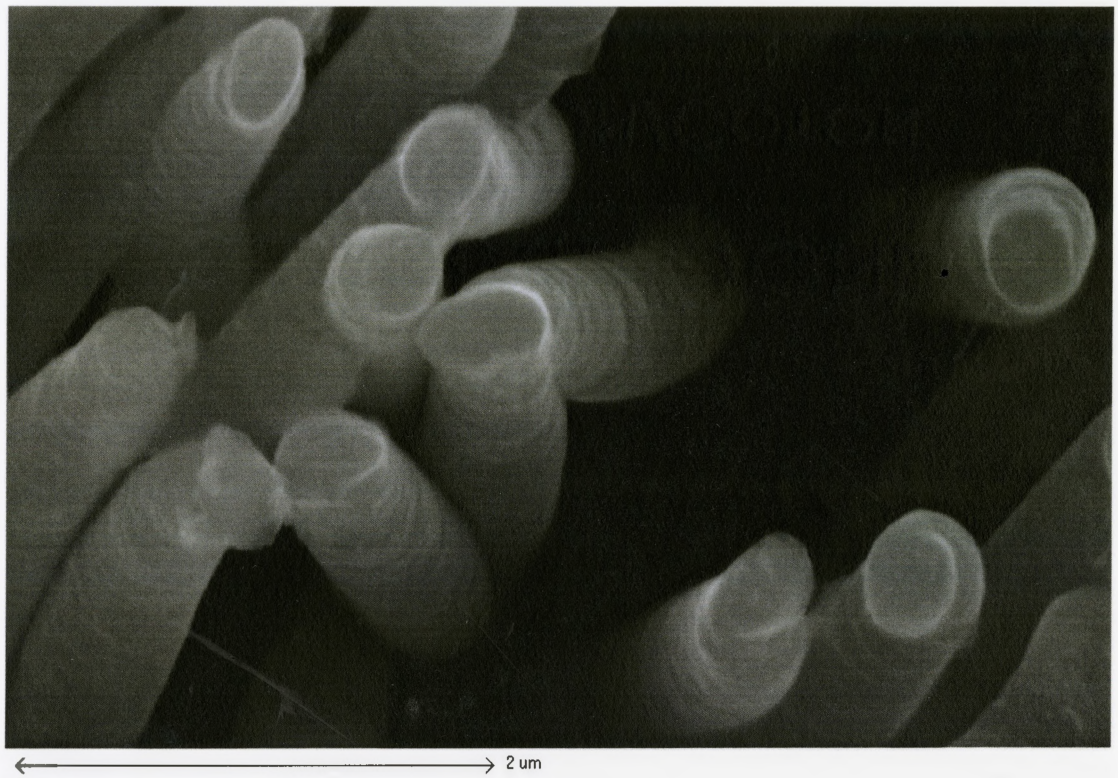

Figure 4.5 Scanning electron micrograph of upright free nanocylinders which were template-synthesized within the pores of a 400 nm polycarbonate membrane.

Edge-on SEM images show the ruptured polycarbonate membrane, the polypyrrole surface layers, and the nanocylinders, sometimes torn, running perpendicular to the surface layers (Figures 4.6 - 4.7). All of these features are visible in low-magnification images (Figure 4.6). At higher magnifications (Figure 4.7), the detailed structure of the nanocylinders can be observed.

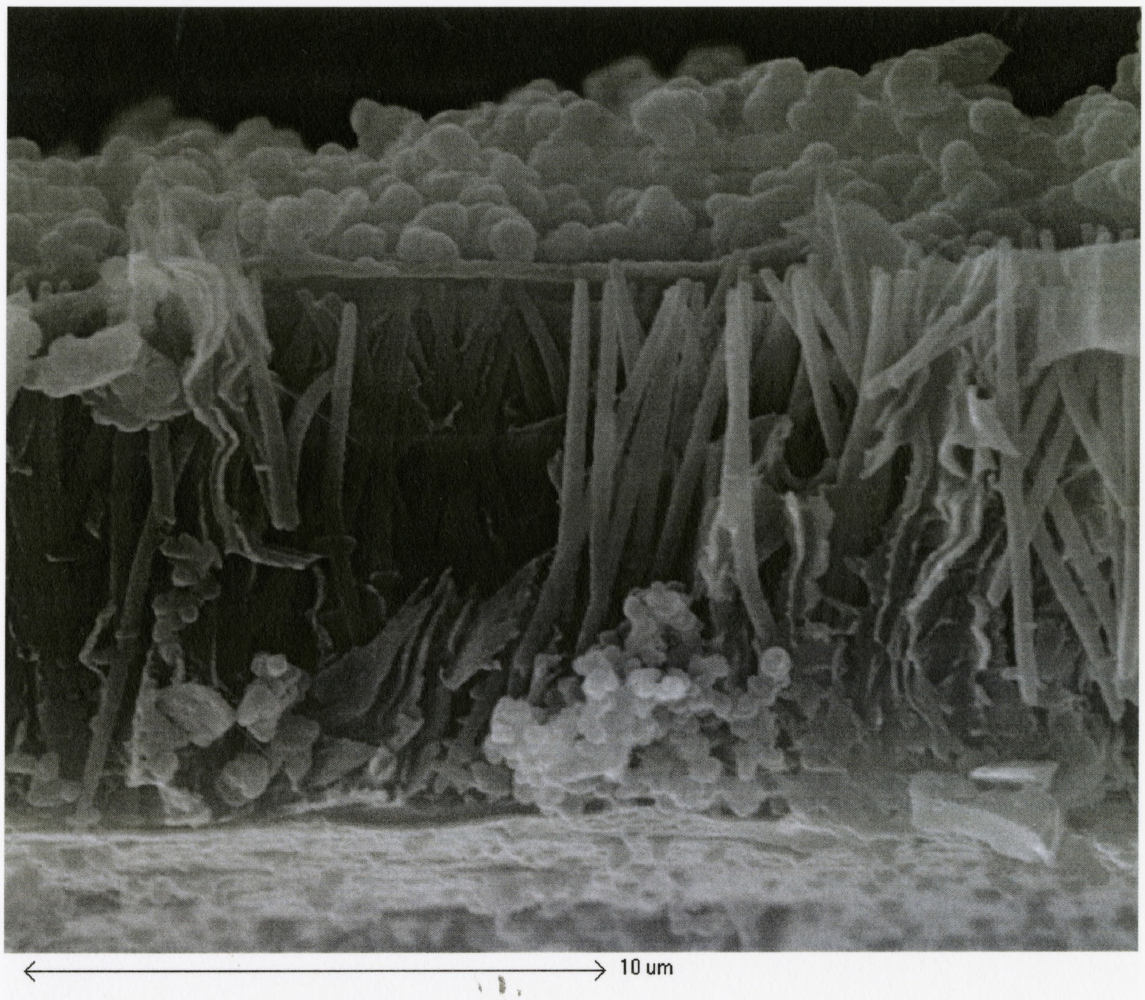

Figure 4.6 Edge-on scanning electron micrograph of a polypyrrole-filled 200 nm polycarbonate membrane.

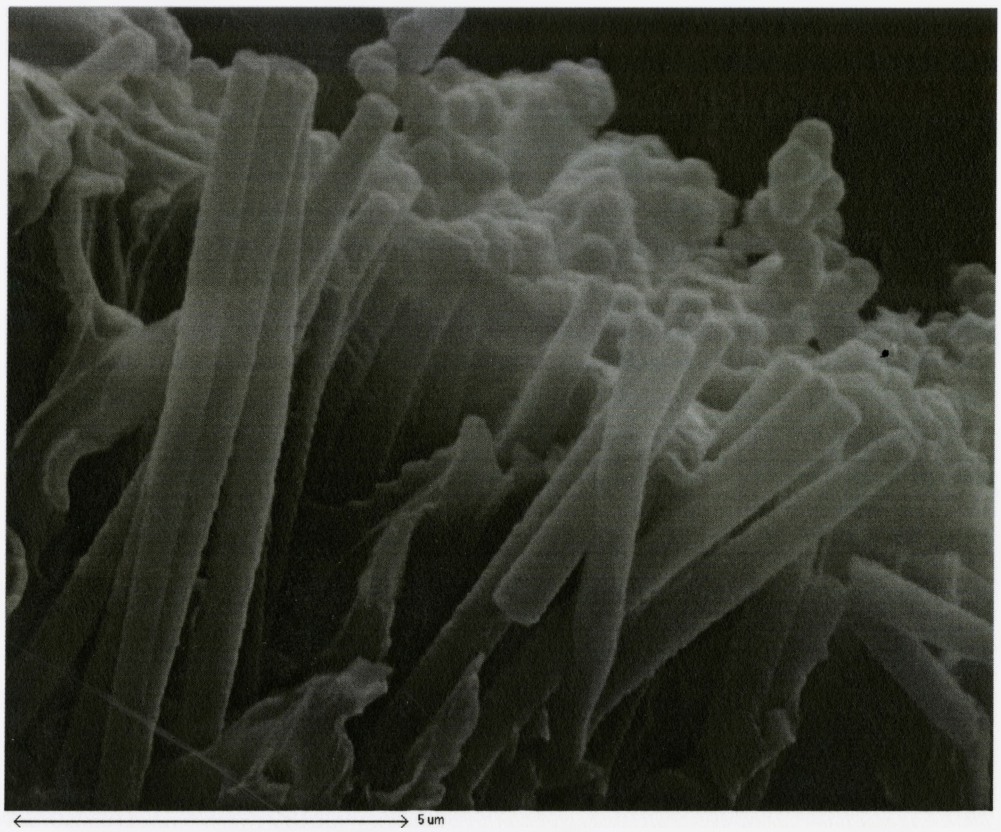

Figure 4.7 Scanning electron micrograph of polypyrrole nanocylinders, exposed by tearing the 400 nm polycarbonate template membrane.

A detailed view of the nanocylinders' internal structure was provided by transmission electron microscopy. Hollow regions of the nanocylinders are clearly indicated by their dark appearance on the micrographs. Figure 4.8 shows a typical view of a group of nanocylinders.

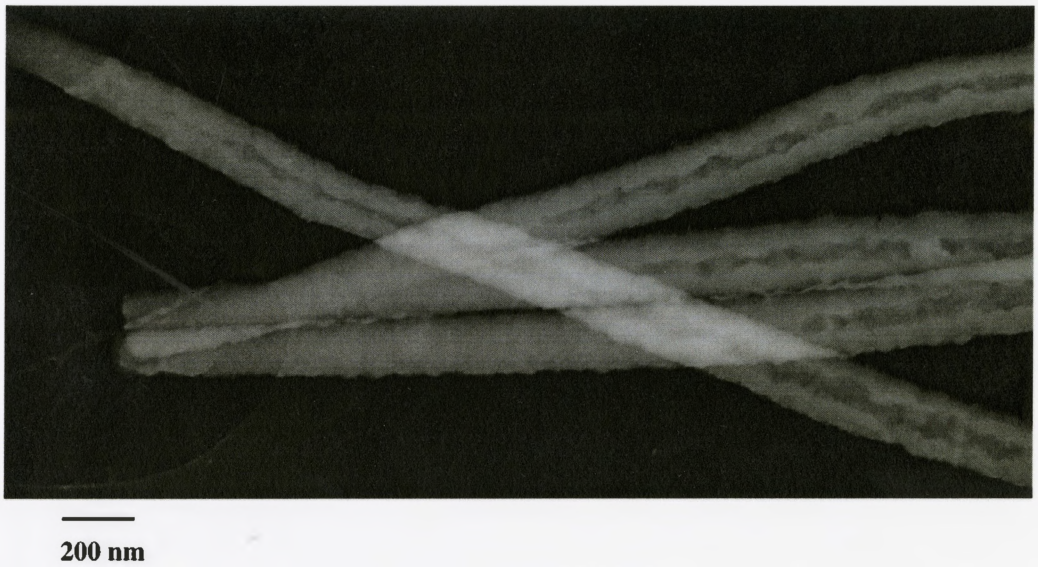

Figure 4.8 Transmission electron micrograph of some freed nanocylinders which were template-synthesized in a 100 nm polycarbonate membrane.

The nanocylinders formed after a 120 minute polymerization time within the pores of polycarbonate membranes of differing diameters had several common characteristics. Tapering near the ends was a ubiquitous feature among

the nanostructures. Striations, running perpendicular to the axes of the nanocylinders, were visible in scanning electron micrographs. The striations are clearly visible on the 400 nm nanocylinders shown in Figure 4.5. The smaller diameter nanocylinders also exhibited this feature, though the pattern was more difficult to resolve. Another common feature was end-to-end growth; i.e., the structures traversed the entire length of the template pores. This conclusion is based on the fact that no truncated nanocylinders, other than those that had jagged breaks due to the preparation for microscopy, were observed. Moreover, the robust growth of the polypyrrole within the polycarbonate membranes' pores suggests a strong likelihood that all of the template's pores were filled.

The dimensions of the nanocylinders, measured from transmission electron micrographs and scanning electron micrographs, are given in Table 4.2. These measurements were performed by using Adobe Photoshop 5.0 to count the number of pixels spanning the features of interest on the micrographs. Distances were converted to conventional units by taking into account the number of pixels per inch on the digital micrograph and the image magnification. The dimensions given in Table 4.2 are averages based on the measurement of dozens of different nanocylinders. The uncertainty ranges reflect the degree of variation among the nanocylinders, which exceeded the precision of the measurements. Because the full lengths were visible in but a few specimens, the average nanocylinder lengths were calculated based on the measured membrane

thickness and the assumption that the angular distribution of pores was isotropic. It should be recalled that the pores are distributed up to $\pm 34^{\circ}$ with respect to the membrane surfaces' normal (Demoustier-Champagne and Stavaux, 1999). The details of the length calculations are given in the Appendix, in section A.1. Measured lengths were within the expected range of values. It should also be noted that, for reasons to be explained at the end of this section, transmission electron micrographs were favored over scanning electron micrographs for most of the measurements.

Table 4.2 Measured nanocylinder dimensions.

Nominal Diameter (nm)	Outer Diameter in Middle Region (nm)	Inner Diameter in Middle Region (nm)	Outer Diameter at Ends (nm)	Length (μm)	Length of Taper (μm)
50	156 ± 20	0	62 ± 15	6.4 ± 0.4	1.2 ± 0.3
100	203 ± 20	63 ± 10	112 ± 15	6.4 ± 0.4	1.3 ± 0.3
200	324 ± 25	114 ± 20	206 ± 20	10.6 ± 0.6	1.7 ± 0.5
400	622 ± 40	247 ± 35	405 ± 35	10.6 ± 0.6	2.0 ± 0.5

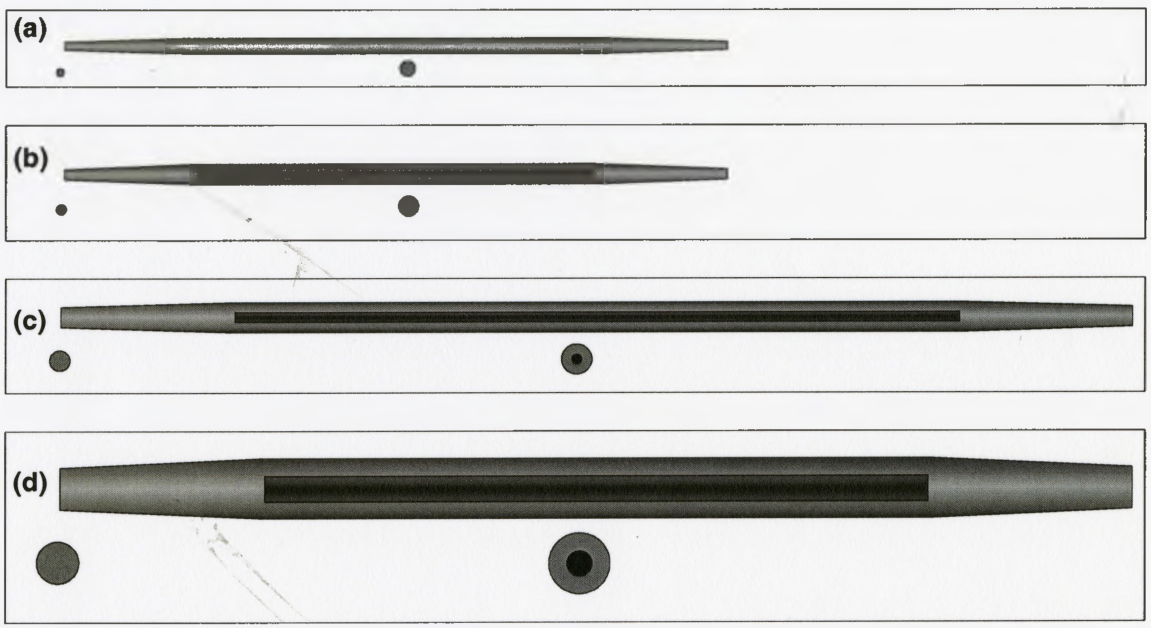

Figure 4.9 Scale-drawing of archetypal nanocylinders. Transverse cross sections at the end and middle regions are shown below the longitudinal cross sections. Black represents hollow areas. The nominal diameters are **(a)** 50 nm, **(b)** 100 nm, **(c)** 200 nm, and **(d)** 400 nm.

An illustrative representation of archetypal nanocylinders, based on the measured dimensions, is given in Figure 4.9. The basic shape is that of a cylinder of roughly uniform diameter capped at either end by a truncated cone. With the exception of the solidly filled 50 nm nanocylinders[1], away from the ends, the nanocylinders were tubular in nature. Nevertheless, the diameter of the hollow regions were relatively small, and since the volume of the tubular hollow goes as the radius squared, the void represents a small proportion of the total volume (about 10%, 12%, 16% for 100 nm, 200 nm, and 400 nm nanocylinders respectively). The diameters at the ends of the nanocylinders were nearly the same size as the nominal pore diameters provided by the membrane manufacturer. In the middle regions, the diameters were much larger than the nominal ones. This discrepancy was more pronounced for the smaller diameter nanocylinders. More specifically, the ratio of the diameter at the middle to the diameter at the ends is about 2.5, 1.8, 1.6, and 1.5 for the nominally 50 nm, 100 nm, 200 nm, and 400 nm nanocylinders. Thus, results based on the use of the nominal pore diameters are questionable, especially for the smallest diameters where the true diameters deviate from the nominal ones by the largest factor.

[1] For the sake of simplicity, nanocylinders which have a nominal diameter of "x" nm will be referred to as an "x" nm nanocylinder.

The template-synthesized nanocylinders were not all alike. Some variation in diameter, filling, and shape was observed. See, for example, Figures 4.7 and 4.8. Other differences between nanocylinders were due to defects. One defect is the growth of protruding nodules. A nanocylinder with several protuberances can be seen in Figure 4.10. These defects appear to be a result of isolated voids in the polycarbonate which constitutes the templates. Another defect is the cross-over of nanocylinders (Figure 4.11) which is due to the intersection of the templating pores. Because the pores are not all parallel, they may intersect; although they only do so rarely.

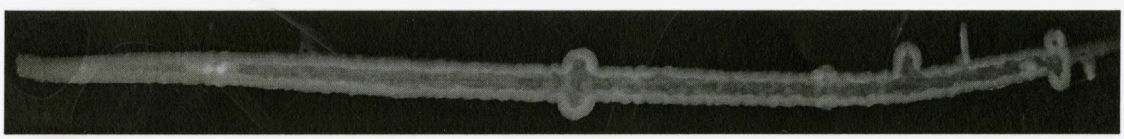

Figure 4.10 Transmission electron micrograph of a 200 nm nanocylinder with several outgrowing nodules.

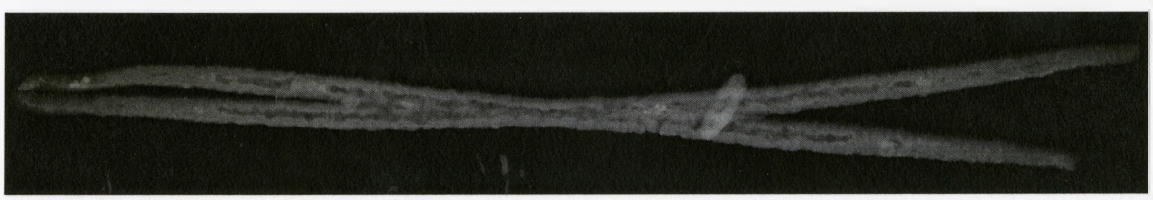

Figure 4.11 Transmission electron micrograph of two intersecting nanocylinders.

The observed nanocylinder structure is consistent with the report of Duchet *et al.*: the nanocylinders were cigar-shaped, with striations covering the surfaces. The presence of nodules and cross-overs were not addressed in any known reports. All of these features reflect the shape of the templating polycarbonate membrane pores. In contrast with Duchet *et al.*, a higher degree of filling was achieved. Filling of 86% - 100% in the middle regions and 100% at the ends were obtained. Duchet *et al.* reported about 65% filling (Duchet *et al.*, 1998). It seems reasonable to postulate that after a somewhat longer reaction time, all diameter polycarbonate membranes would fill entirely, forming solid nanofibrils. As evidenced by the investigation of the filling in 50 nm polycarbonate membranes, the degree of filling is directly related to the reaction time. It is likely that the larger diameter nanocylinders were not completely filled because filling a larger volume requires more polymer growth, and hence, a longer polymerization time. This reasoning is the same as that used in section 4.1.1 for explaining why the ends of the 50 nm nanocylinders filled in entirety before the middle regions.

Transmission electron micrographs were favored over scanning electron micrographs for the measurement of the nanocylinder dimensions for several reasons. First of all, the resolution of the TEM was superior to that of the SEM. Secondly, unlike the SEM imaging, the TEM imaging did not require the deposition of a thin gold coating. Inevitably, the presence of a gold layer affects the measured dimensions. Nevertheless, the SEM was adequate for the

measurement of the lengths, taper-lengths, and the outer diameters for the larger diameter nanocylinders. For the measurement of the inner nanocylinder diameters, the TEM was favored because it provides far more information than the SEM about the internal structure of the nanocylinders. Furthermore, as a result of simple geometrical considerations, the TEM is capable of sharply delineating the hollow regions. Where the nanocylinder is hollow, less material has to be traversed by the TEM's electron beam (Figure 4.12 (a)). The abrupt change in the amount of material to traverse results in an abrupt change in the intensity registered by the TEM (Figure 4.12 (b)). Edge-on SEM images may also be used to measure the inner diameters, since the membrane-breaking process severed many of the nanocylinders, leaving transverse cross sections of the nanocylinders exposed. Nevertheless, many cross sections would have to be observed in order to get a sense of the overall internal structure. Unfortunately, the nanocylinders were often lying at an angle and the cross section could not be measured. On occasion, the cross sections were in plain view (Figure 4.13) and were measured to corroborate the TEM results. Duchet *et al.* (Duchet *et al.*, 1998) and Demoustier-Champagne and Stavaux (Demoustier-Champagne and Stavaux, 1999) used an SEM to measure the inner diameters of the nanocylinders at the ends. This measurement is deficient since the cross section at the ends may not be representative of the cross sections elsewhere.

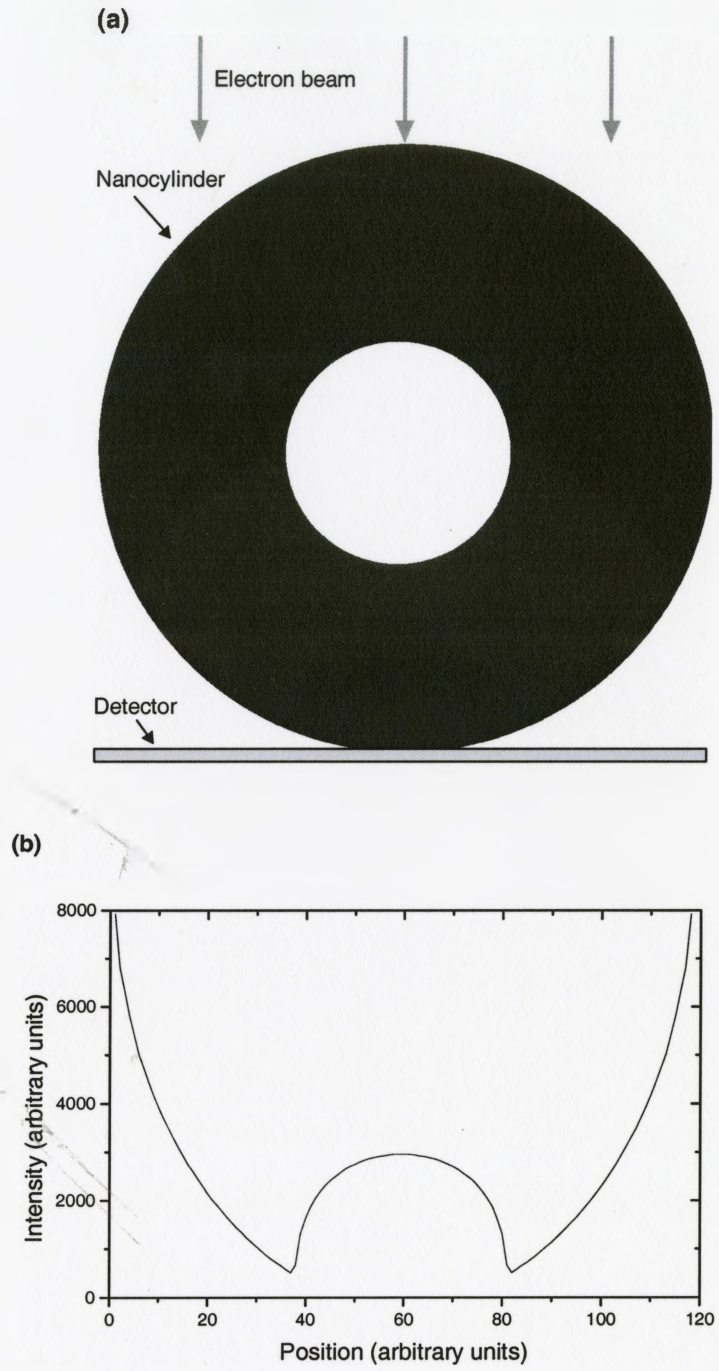

Figure 4.12 **(a)** Schematic representation on an electron beam impinging on a nanocylinder and an electron detector, and **(b)** the corresponding electron intensity pattern registered by the detector.

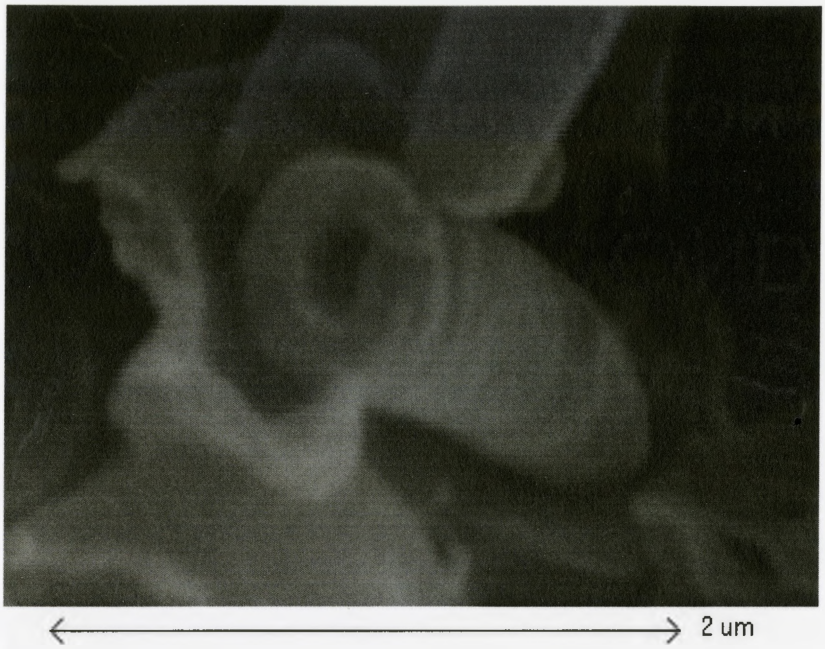

Figure 4.13 Scanning electron micrograph of a severed polypyrrole nanocylinder, exposed by tearing a 400 nm polycarbonate template membrane.

4.1.3 Alumina Membrane-Templated Polypyrrole Nanocylinders

The morphology of polypyrrole nanostructures grown within the pores of alumina membranes over the course of a 120 minute reaction time were investigated by scanning electron microscopy and transmission electron microscopy. An edge-on scanning electron micrograph of a filled 100 nm alumina template and a transmission electron micrograph of freed 100 nm alumina membrane-templated nanostructures are shown in Figures 4.14 and 4.15 respectively. Similar SEM and TEM images are shown for 20 nm structures in Figures 4.16 and 4.17 respectively.

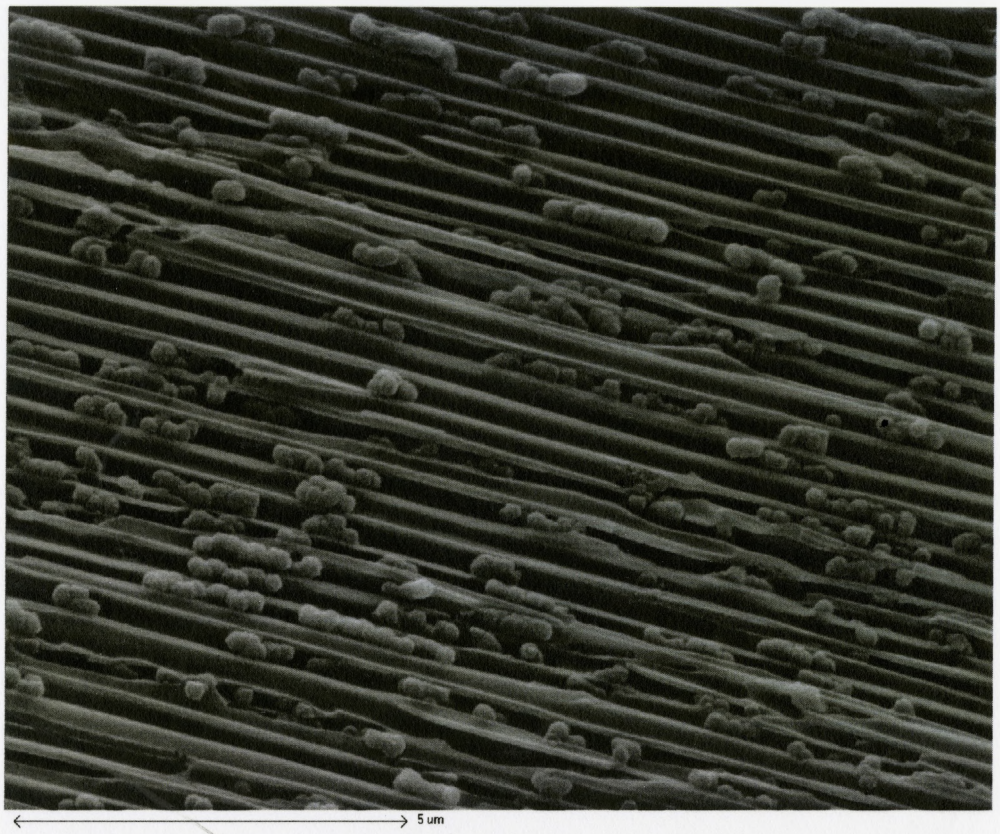

Figure 4.14 Edge-on scanning electron micrograph of a polypyrrole-filled 100 nm alumina membrane.

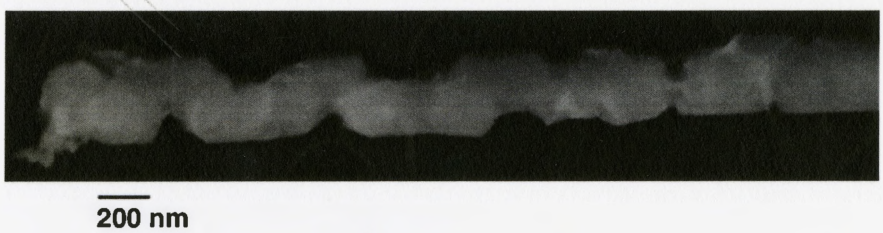

Figure 4.15 Transmission electron micrograph of a freed nanocylinder which was template-synthesized in a 100 nm alumina membrane.

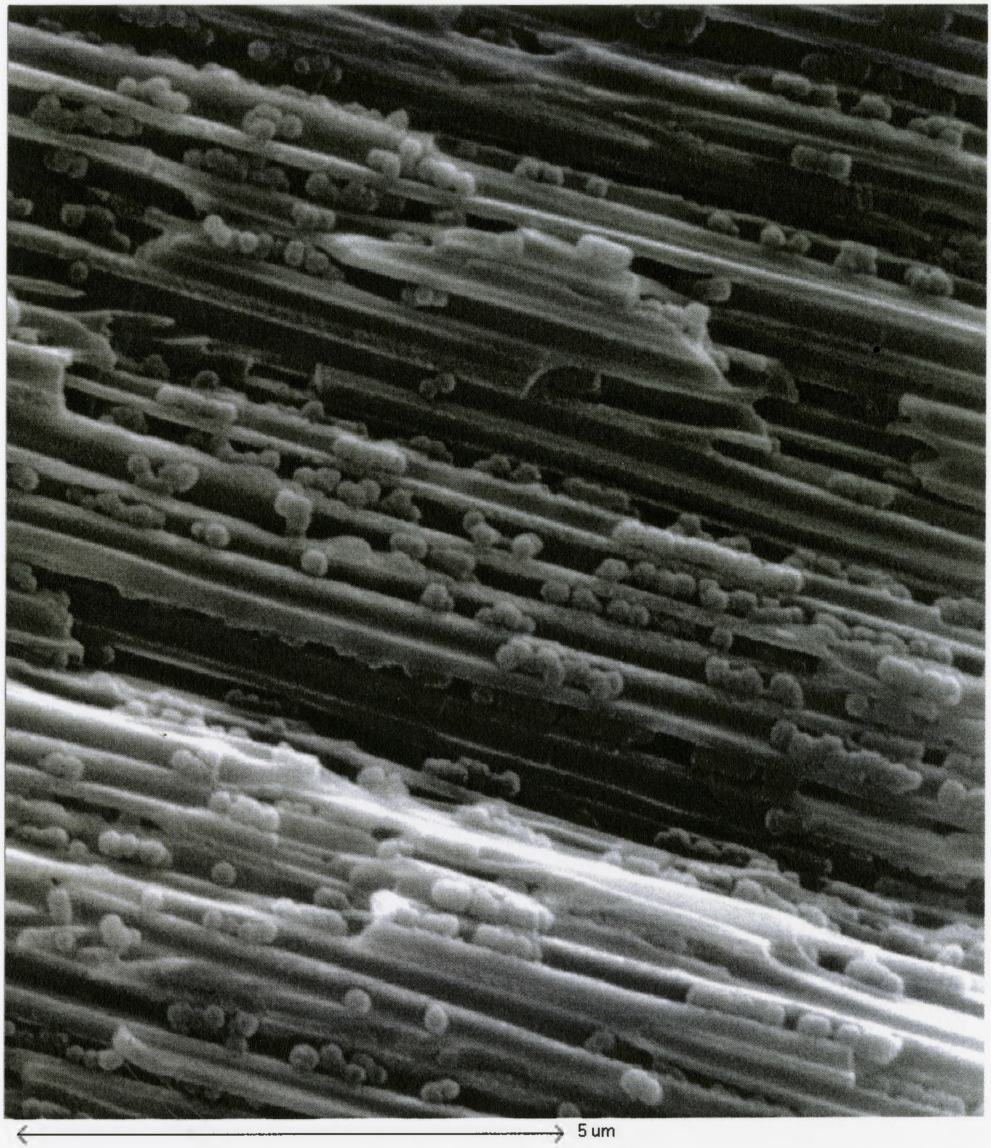

Figure 4.16 Edge-on scanning electron micrograph of a polypyrrole-filled 20 nm alumina membrane.

Figure 4.17 Transmission electron micrograph of two freed nanostructures which were template-synthesized in a 20 nm alumina membrane.

The basic morphology of the alumina membrane-templated nanostructures is that of a linear aggregate of irregularly shaped blobs. For the structures which were templated in 100 nm pores, the blobs measured 290 ± 50 nm across, had an elongated shape and were packed closely together. The nominally 20 nm structures were made up of quasi-spherical blobs, measuring 116 ± 20 nm across, and were held together by tenuous connecting regions measuring 56 ± 15 nm across. The nanostructures shown in Figures 4.14 - 4.17

are fragmented. This is partially due to the process used for preparing the samples for microscopy, which may cause the weakly linked blobs to separate. Furthermore, following polypyrrole synthesis, only a small proportion of the nanostructures were connected from end-to-end of the templating membrane. This latter point is supported by the resistance data (section 4.2.2), which showed that despite having a resistivity which was comparable to that of the polycarbonate membrane-templated nanocylinders, the trans-membrane resistance for a given contact area was a fair amount higher (about 1000 times higher). According to the equation which relates resistivity to resistance, this indicates that the effective contact area was far less, or, in other words, fewer end-to-end nanostructures were contacted for the case of the alumina membrane-templated samples.

The marked difference in morphology between the alumina membrane-templated nanostructures and the polycarbonate membrane-templated nanostructures reflects a difference in the surface chemistry taking place at the pore walls. As mentioned in section 2.4.1, the polycarbonate pore walls have anionic sites which are residual from the track-etching process used to form the pores. These sites act as *molecular anchors* (Martin, 1994) which bind to the nascent cationic polypyrrole. Consequently, the polypyrrole preferentially nucleates along the pore walls, and grows to form a continuous coating along the pore walls. No such molecular anchor sites are present on the alumina pore

walls. Hence, there is no preferential growth along the pore walls; instead, the nucleation appears to be at random positions within the pores. The polypyrrole subsequently grows radially outward from the nucleation site, until a pore wall or another polypyrrole mass is contacted. Once in close proximity, the blobs can grow together.

4.2 Resistivity

4.2.1 Polycarbonate Membrane-Templated Polypyrrole Nanocylinders

The resistance[1] across polypyrrole-filled polycarbonate membranes was measured as a function of temperature. A 120 minute polymerization time was used to prepare the samples. Figure 4.18 shows a typical plot of the temperature-dependence of the resistance between room temperature and 5 K. Over this temperature range, the nanocylinders exhibited semiconducting behavior; i.e., the resistance increased with decreasing temperature.

[1] Since resistance and resistivity are related by geometrical factors, temperature-dependence of the same form is obeyed by the two quantities. In analyzing the data, resistance was favored over resistivity in order to consider the data in as unaltered a form as possible.

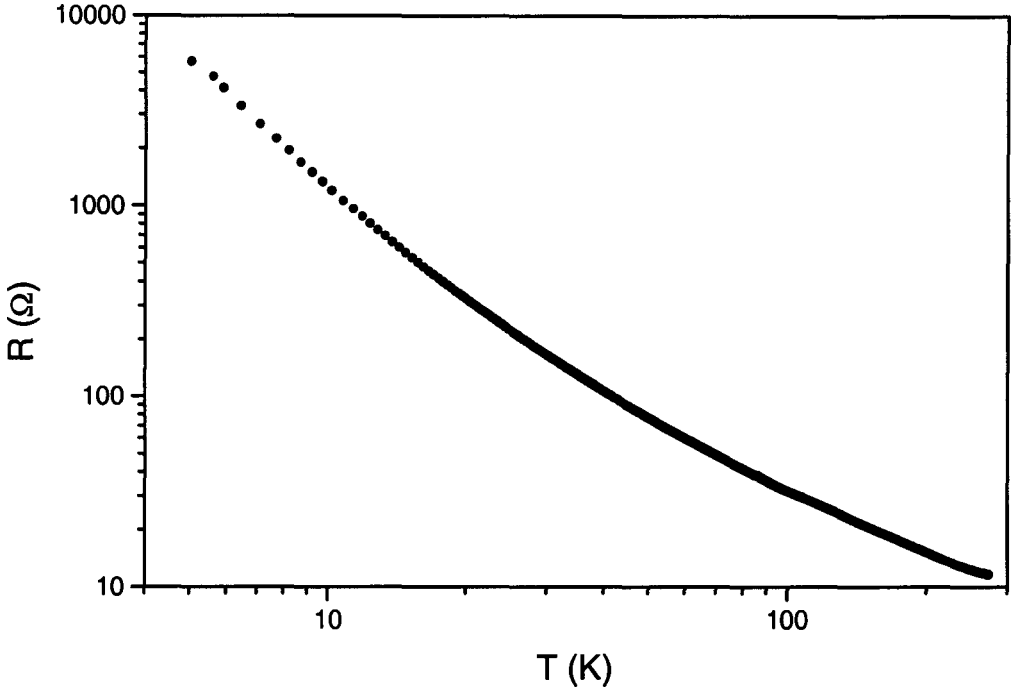

Figure 4.18 Log-log plot of the trans-membrane resistance R as a function of temperature T for a polypyrrole-filled 50 nm polycarbonate membrane.

In order to determine whether Mott or Efros-Shklovskii variable range hopping was obeyed, the logarithm of the reduced local activation energy, *w*, was plotted as a function of the logarithm of temperature (see section 2.2.4). A representative graph, derived from the same data as Figure 4.18, is shown in Figure 4.19. The slope of this type of plot, at sufficiently low temperatures, yields the exponent *x* in the general expression for the variation of resistivity with

temperature, equation 2.10. For three, two, or one-dimensional Mott variable range hopping, x is expected to be 1/4, 1/3, or 1/2, respectively. For Efros-Shklovskii variable range hopping, x is expected to be 1/2. Over the 300 K - 5 K temperature range, all of the samples yielded a value of x with an uncertainty range which overlapped 1/4. The average value for x was 0.25 ± 0.02. This strongly suggests that between 300 K and 5 K, three dimensional Mott variable range hopping was the conduction mechanism for every investigated nanocylinder diameter. For all of the samples, the linear dependence of $\ln(R)$ on $T^{-1/4}$, characteristic of Mott variable range hopping, was obtained. This dependence is shown for one sample in Figure 4.20, using the same data as Figures 4.18 and 4.19.

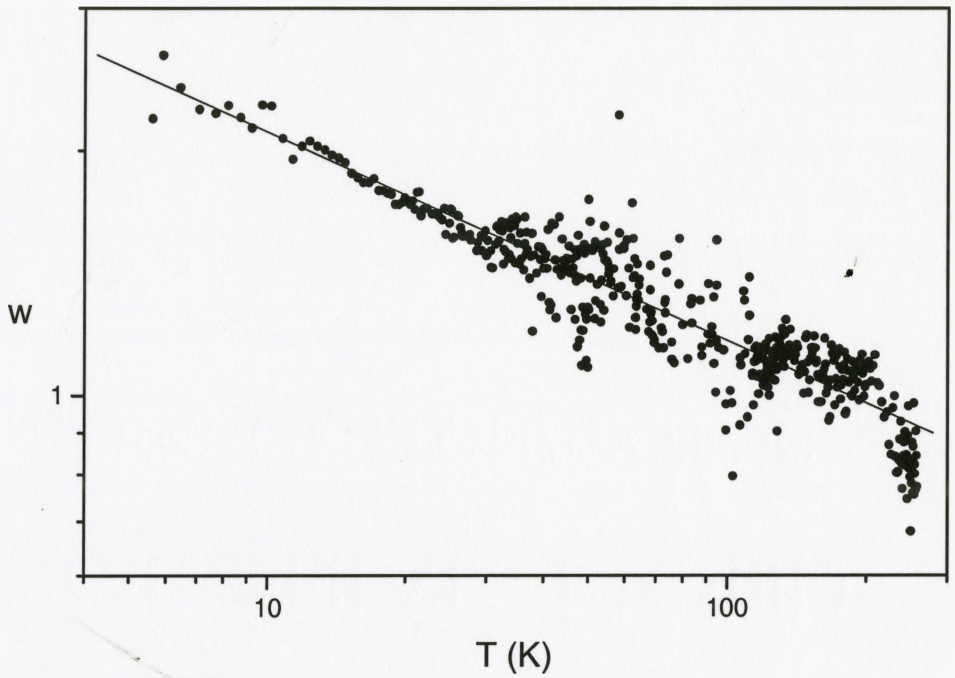

Figure 4.19 Log-log plot of the reduced local activation energy *w* as a function of temperature T for a polypyrrole-filled 50 nm polycarbonate membrane. The solid line is the line of best-fit.

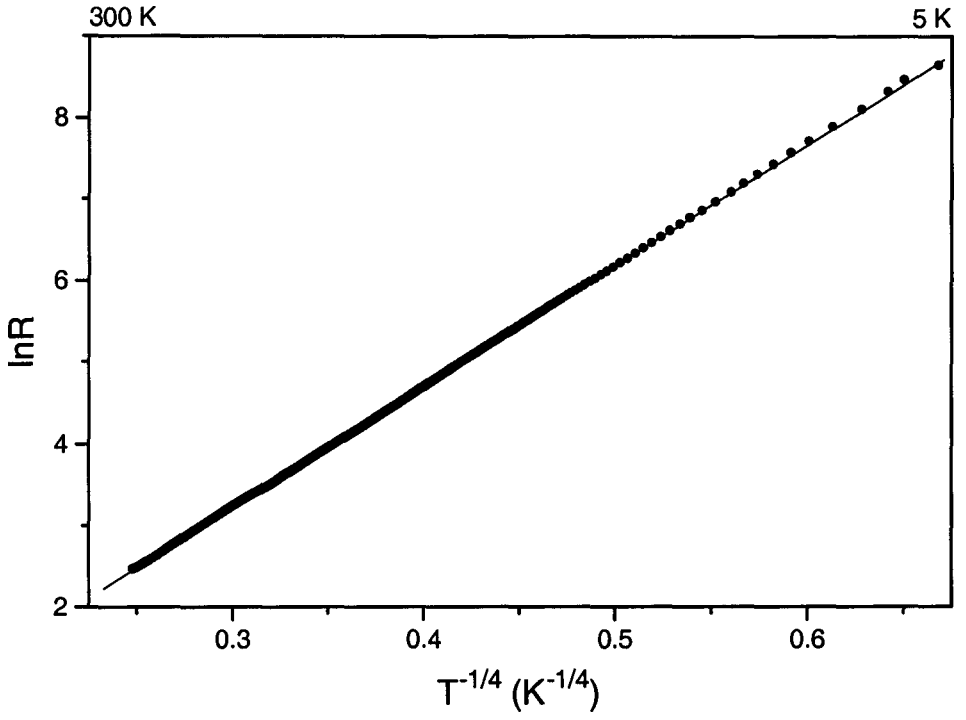

Figure 4.20 Plot of ln$R$ versus $T^{-1/4}$ for a polypyrrole-filled 50 nm polycarbonate membrane. The solid line is the line of best-fit.

The value of the Mott characteristic temperature T_0 for the nanocylinders was determined from the slope of the ln$R$ versus $T^{-1/4}$ graphs. A summary of the T_0 values obtained for each nanocylinder diameter is provided in Figure 4.21. Each data point represents an average value, obtained from measurements performed on two or three separate samples. The value of T_0 is larger for the smaller diameter nanocylinders. In general, larger values of T_0 correspond to

smaller values of conductivity, since T_0 is inversely related to the localization length and the density of states at the Fermi level (section 2.2.1). Therefore, contrary to the results of Cai *et al.* (Cai *et al.*, 1991), Duchet *et al.* (Duchet *et al.*, 1998), Demoustier-Champagne and Stavaux (Demoustier-Champagne and Stavaux, 1999), the T_0 data suggest that the conductivity is lower for the smaller diameter nanocylinders.

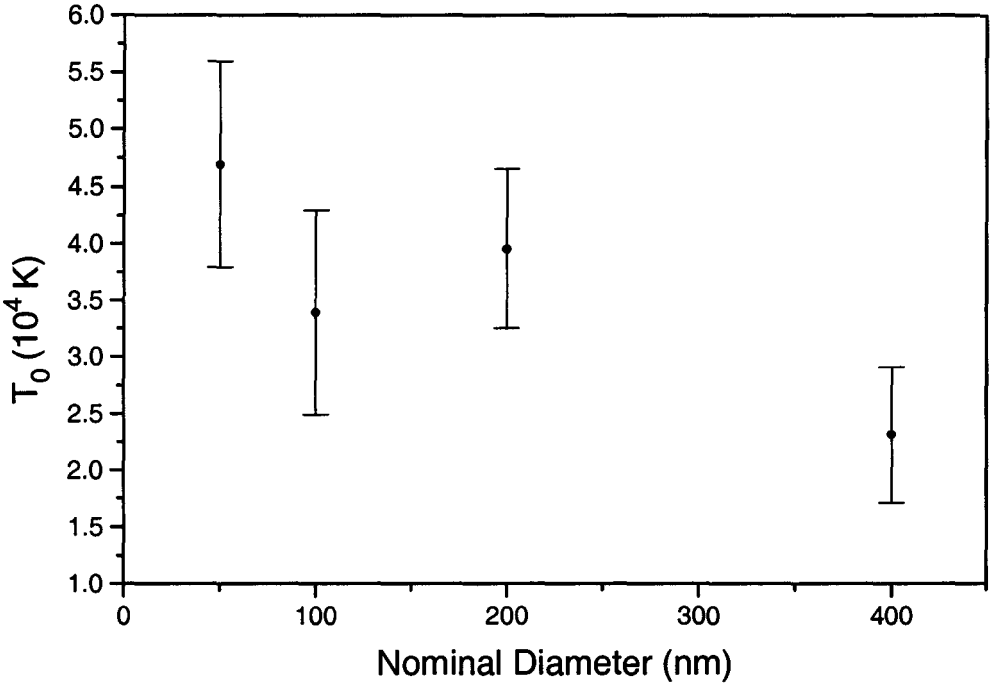

Figure 4.21 Mott characteristic temperature T_0 versus nominal nanocylinder diameter.

The room temperature conductivity for each diameter nanocylinder was carefully measured. The calculations were performed by taking into account the detailed morphology of the nanocylinders. It was established in section 4.1.2 that the nanocylinders were far from being uniformly cylindrical. Instead, they were composed of a roughly tubular or fibrillar section in the center and solid tapering regions at the ends. This geometry is reasonably well approximated by a tube or fibril capped at the ends by truncated cones, as depicted in Figure 4.9. The resistivity ρ for this geometrical arrangement is

$$\rho = \pi n A R \left[\frac{2\ell}{r_e r_o} + \frac{L}{\left(r_o^2 - r_i^2\right)} \right]^{-1}, \qquad (4.1)$$

where n is the pore density, A is the contact area, R is the trans-membrane resistance, r_i is the inner nanocylinder radius in the middle region, r_o is the outer nanocylinder radius in the middle region, r_e is the nanocylinder radius at the ends, ℓ is the taper length, and L is the nanocylinder length. A derivation of equation 4.1 is given in the Appendix, in section A.2. The electrical contact area was measured using the procedure outlined in section 3.3.1. The nanocylinder dimensions were measured by TEM and SEM and are provided in Table 4.2 in section 4.1.1.

The conductivity of the various diameter nanocylinders is shown in Figure 4.22. Each data point is an average value based on measurements of two or three separate samples. There is a modest drop in the conductivity as the diameter of the nanocylinder is decreased. These results are consistent with the T_0 data and provide corroborative evidence for a slightly diminished conductivity in the smaller diameter nanocylinders.

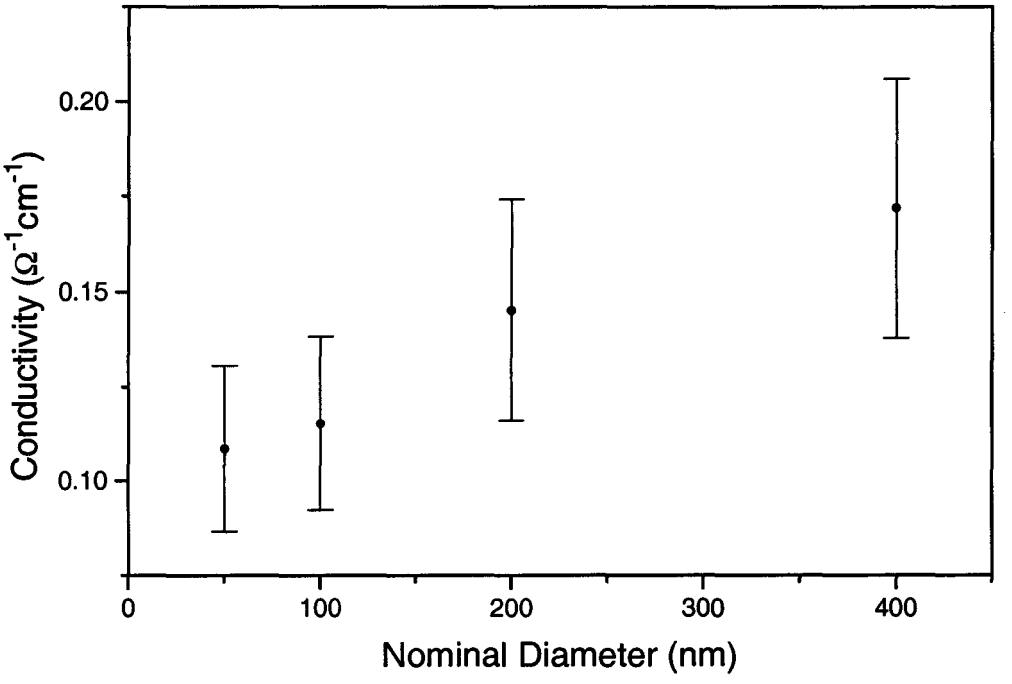

Figure 4.22 Nanocylinder conductivity versus nominal nanocylinder diameter.

It should be noted that for measuring the relative conductivities of template-synthesized nanostructures, the determination of the Mott characteristic temperatures T_0 may be more reliable than direct measurements of the conductivities. The use of T_0 circumvents the problem of having to characterize the morphology of the nanostructures. The measurement is independent of the filling factor and the size of the contact areas as well. Moreover, structures with highly complex and irregular shapes, such as those templated in the alumina membranes (section 4.1.3), may be considered. Finally, since T_0 is determined directly from the raw temperature-dependence of the resistance, the greatest source of error in the measurement is sample-to sample-variation.

The Oxford measurement system was used to measure the temperature dependence of the trans-membrane resistance between 10 K and 1.8 K. Figure 4.23 shows a typical graph of resistance versus temperature for these lower temperatures. As for the higher temperature measurements, semiconducting behavior was observed. A log-log plot of the reduced local activation energy as a function of temperature is shown in Figure 4.24. For all of the samples measured, a transition was observed at 5 ± 1 K, where the slope changes from 0.25 ± 0.02 at higher temperatures to 0.48 ± 0.05 at lower temperatures. This suggests that at low temperatures, the conduction mechanism is either Efros-Shklovskii variable range hopping or one-dimensional Mott variable range hopping. The resistivity experiment cannot differentiate between the two hopping mechanisms.

However, based on the magnetoresistance data, it is argued in section 4.3.1 that the former case is more likely than the latter. Plots of ln(R) versus $T^{-1/4}$ and ln(R) versus $T^{-1/2}$ over the 10 K - 1.8 K temperature range are shown in Figures 4.25 and 4.26 respectively. The linear dependence of ln(R) on $T^{-1/4}$ between 10 K and 5 ± 1 K indicates that three-dimensional Mott variable range hopping is valid for these temperatures, while the linear dependence of ln(R) on $T^{-1/2}$ between 5 ± 1 K and 1.8 K indicates that Efros-Shklovskii or one-dimensional Mott variable range hopping is valid at low temperatures.

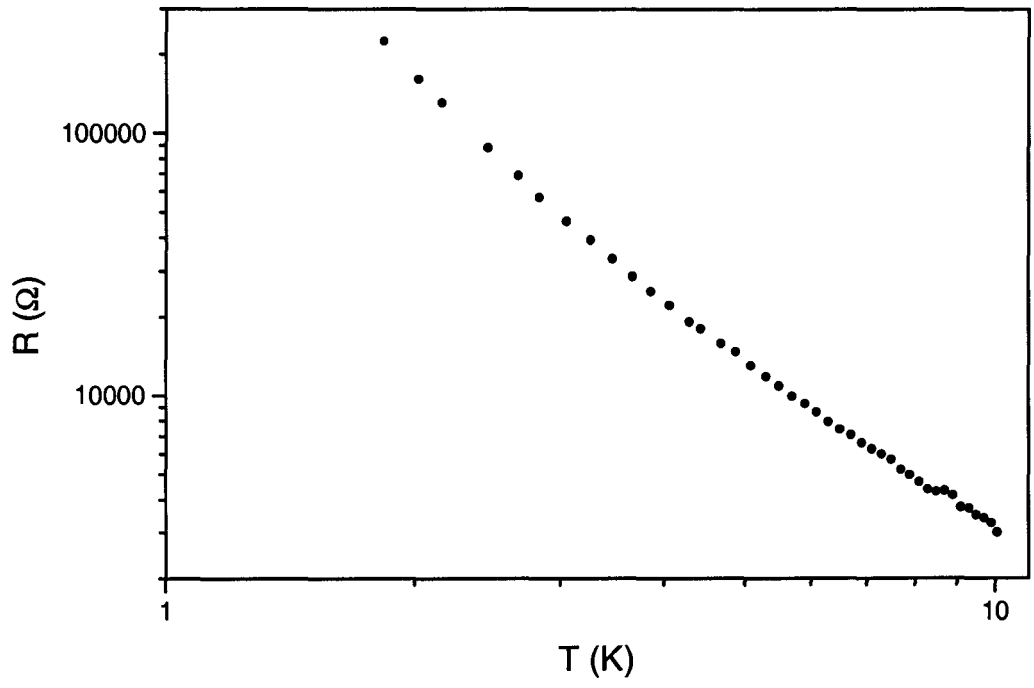

Figure 4.23 Log-log plot of the trans-membrane resistance R as a function of temperature T for a polypyrrole-filled 100 nm polycarbonate membrane.

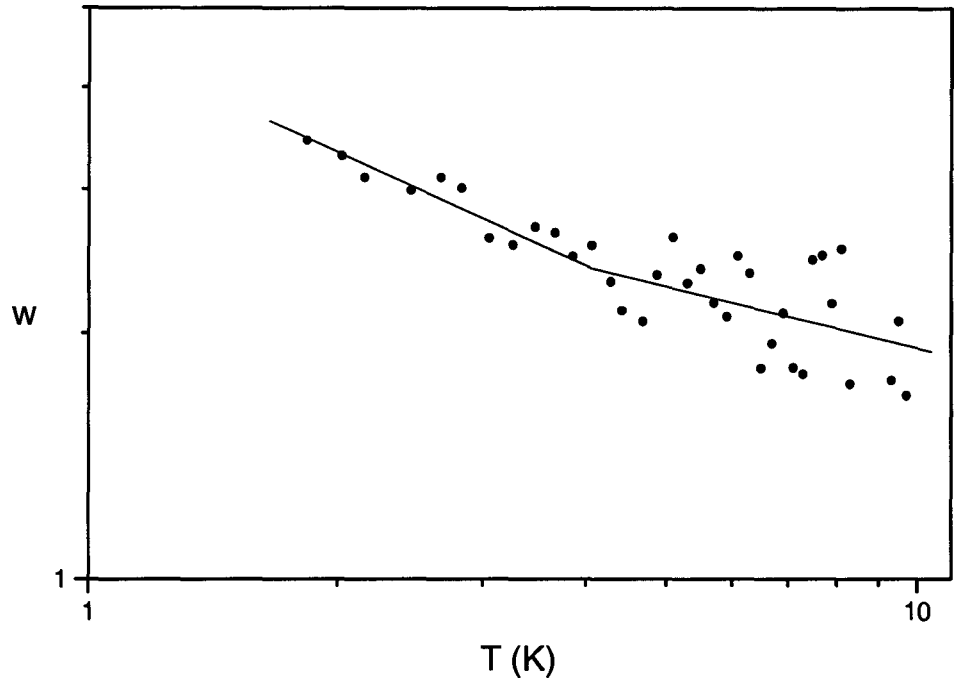

Figure 4.24 Log-log plot of the reduced local activation energy *w* as a function of temperature T for a polypyrrole-filled 100 nm polycarbonate membrane. The solid lines are the lines of best fit over the temperature regions above and below 5 K.

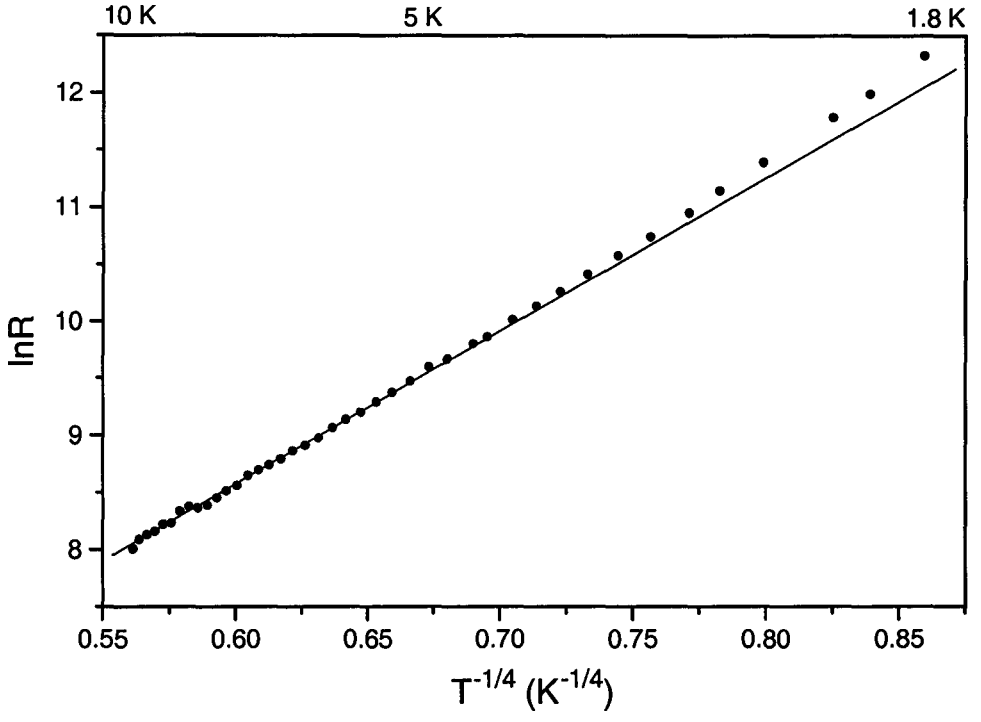

Figure 4.25 Plot of ln$R$ versus $T^{-1/4}$ for a polypyrrole-filled 100 nm polycarbonate membrane. The solid line is the line of best-fit for temperatures above 5 K.

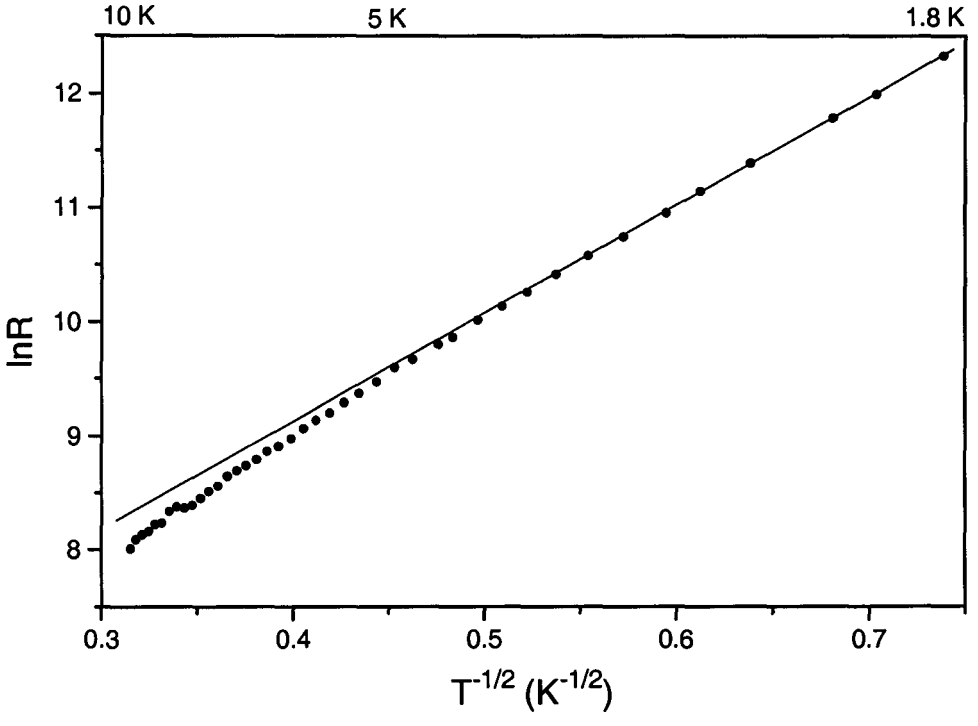

Figure 4.26 Plot of ln$R$ versus $T^{-1/2}$ for a polypyrrole-filled 100 nm polycarbonate membrane. The solid line is the line of best-fit for temperatures below 5 K.

The observed decrease in conductivity with decreasing diameter is at odds with the numerous reports of enhanced conductivity in the smaller diameter nanocylinders. Nonetheless, the contrary results may be reconcilable on account of the notable differences which exist between the analyses of the present study and previous work.

Cai *et al.* (Cai *et al.*, 1991) and Duchet *et al.* (Duchet *et al.*, 1998) treated the nanocylinders synthesized in commercially fabricated membranes as solid uniformly cylindrical fibrils, having the radius of the pore openings. In light of the cigar-like shape of the nanocylinders, these radius values are underestimates. Since the conductivity of a solid fibril is inversely related to the square of the radius (equation 2.14, section 2.4.2), an underestimate in the radius results in an overestimate in the calculated conductivity. It was shown in section 4.1.2 that the discrepancy between the middle and end radii is more pronounced for the smaller radius nanocylinders. Hence, for the smaller radius nanocylinders, the overestimate in the calculated conductivity is more severe. This can be seen in Figure 4.27, where the conductivity of the nanocylinders was calculated by treating the nanocylinders as solid fibrils with the radii given by the nominal pore radii, which are within the uncertainty ranges of the measured end radii (Table 4.2, section 4.1.2). The apparent steep increase in conductivity with decreasing nanocylinder diameter is similar to that reported by Cai *et al.* and Duchet *et al.* The presence of hollow regions may also affect the conductivity calculations.

However, unless the inner radius is comparable to the outer radius, the hollow region represents a small proportion of the total volume due to the dependence of the volume on the square of the radius.

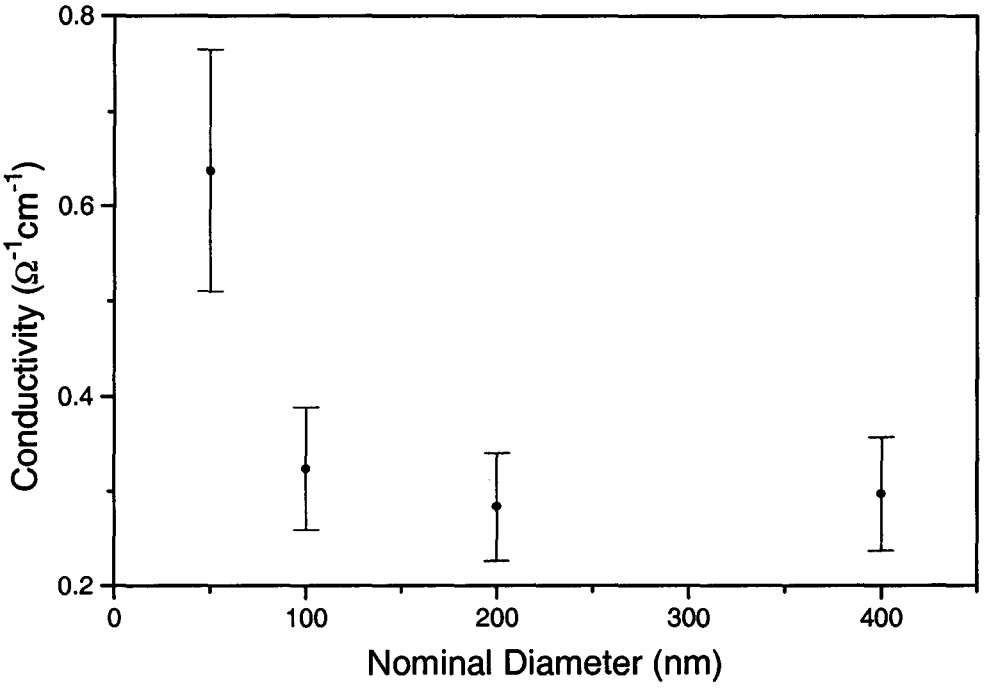

Figure 4.27 Nanocylinder conductivity, calculated based a solid cylindrical morphology and the nominal radii, versus nominal nanocylinder diameter.

Uniformly cylindrical nanostructures were electrochemically synthesized by Demoustier-Champagne and Stavaux (Demoustier-Champagne and Stavaux, 1999) through the use of homemade polycarbonate track-etched membranes as templates. The nanostructures were characterized by field-emission SEM and the tubular nature of the nanocylinders was taken into account in the conductivity measurements. There are multiple procedural differences between their work and the present study which may account for the contrasting observations of the two studies. The electrochemical method results in a large proportion of unfilled template pores. Demoustier-Champagne and Stavaux estimated the number of filled pores by comparing the measured charge consumed after a given electropolymerization time with a theoretical amount. With regards to this method, they state: "Nevertheless, even by doing this correction, incertitude still remains on the exact number of contacted polypyrrole nanotubules," (Demoustier-Champagne and Stavaux, 1999). A second difference between the two works is that the nanotubules produced by their method had very thin walls. For the smallest diameter nanocylinders (35 nm outer diameter) the tubule walls were observed by field-emission SEM to be as thin as 7 nm. It is inevitable that the uncertainty associated with these measurements is large. Moreover, the thickness of the tube walls were measured by viewing the ends of the nanostructures. However, as seen in section 4.1.2, the degree of filling at the ends may not be representative of the filling throughout the rest of the length of the nanocylinders. A further difference in method is related to the polymerization

time. In the present study, a reaction time of 120 minutes was employed for the synthesis of each sample. Demoustier-Champagne *et al.* varied the reaction time significantly, with the polymerization time for the largest diameters being six times longer than that for the smallest diameters. According to Chen *et al.* (Chen *et al.*, 1995), a six-fold increase in polymerization time can lead to a sizable drop in conductivity. However, this study considered chemical synthesis, and it is not clear that the results carry over to the case of electrochemical synthesis. Finally, it was also noticed from a scanning electron micrograph in Demoustier-Champagne and Stavaux' report that a considerable number of the parallel tubules were conjoined, sometimes resulting in highly irregular morphologies.

The present study is in agreement with measurements performed by Orgzall *et al.* on thin films composed of polypyrrole nanotubules. It was observed that the electrical conductivity of films composed of 50 nm nanotubules was lower than that observed in films composed of 400 nm nanotubules (Orgzall *et al.*, 1996). They accounted for the disparity between this result and previous studies by noting that the high degree of porosity in the films may have skewed the results. It should further be noted that it may not be appropriate to directly compare the results of these thin film studies with the results of measurements performed on unprocessed nanocylinders since it seems highly possible that in the case of the films, the inter-tubule resistance dominates over the intrinsic tubule resistance. The latter resistance is the quantity of interest. Moreover, the

compaction process used in making the films may alter the microscopic arrangement of the polymer.

The observations of polypyrrole chain alignment may also be compatible with the resistivity results. It was shown by Cai *et al.* that the polymer chains were aligned along the surfaces of the nanocylinders (Cai *et al.*, 1991) with the preferred orientation perpendicular to the nanocylinders' axes. The observed surface striations may be a reflection of this underlying microstructure. Alignment, however, does not necessarily imply supermolecular order. According to Maddison and Tansley, because the monomer units in polypyrrole chains do not have complete rotational freedom, they cannot be ordered into a crystalline arrangement (Maddison and Tansley, 1992). Furthermore, It is possible that the alignment may be inconsequential in terms of the electrical conductivity. In other words, although the chains were shown to have a preferred orientation, the alignment may not be in such a way as to have a positive effect on the conductivity.

4.2.2 Alumina Membrane-Templated Polypyrrole Nanocylinders

The resistance across a polypyrrole-filled 100 nm alumina membrane was measured as a function of temperature between room temperature and 78 K. A 120 minute reaction time was used to prepare the sample. Much like the polycarbonate membrane-templated samples, the alumina membrane-templated sample exhibited three dimensional Mott variable range hopping behavior. A plot showing the linear dependence of $\ln R$ on $T^{-1/4}$ can be seen in Figure 4.28. The Mott characteristic temperature T_0 was found to be $(3.5 \pm 0.9) \times 10^4$ K. As can be seen in Figure 4.21, this value is in the middle of the uncertainty ranges for the 100 nm and 200 nm polycarbonate-membrane templated nanocylinders. This suggests that the conductivity of the alumina membrane-templated sample is nearly the same as that of the polycarbonate membrane-templated nanocylinders of similar diameter, despite a drastically different morphology which displayed little order. Furthermore, there were no order-inducing molecular anchor sites along the template pore walls. This result supports the argument that there is no conductivity-enhancing order in the polycarbonate membrane-templated nanocylinders.

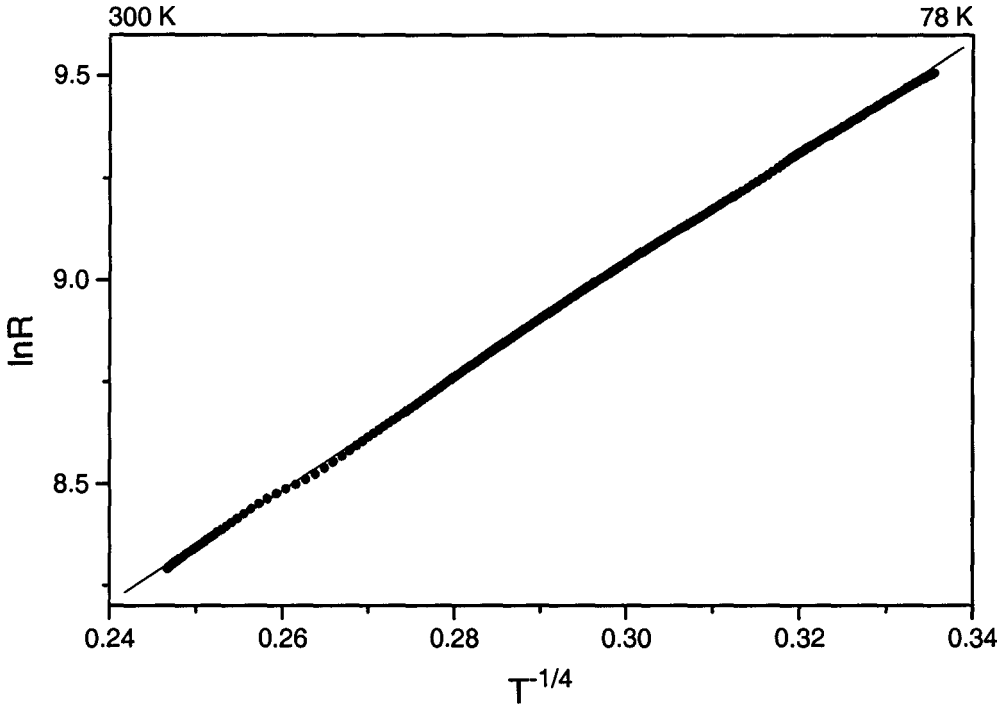

Figure 4.28 Plot of ln$R$ versus $T^{-1/4}$ for a polypyrrole-filled 100 nm alumina membrane. The solid line is the line of best-fit.

It was not possible to determine the absolute conductivity from the trans-membrane resistance measurements owing to the irregular globular nature of the alumina membrane-templated nanostructures. Moreover, it was not known what proportion of the nanostructures extended from end-to-end of the membrane. Nevertheless, based on the results in the previous section and previous reports on hopping conductivity (Maddison and Tansley, 1992; Roth and Bleier, 1987),

the characteristic Mott temperature is a reliable indicator of the electrical conductivity.

4.3 Magnetoresistance

4.3.1 Polycarbonate Membrane-Templated Polypyrrole Nanocylinders

The resistance across polypyrrole-filled polycarbonate membranes was measured in the presence of a transverse magnetic field by using the Oxford measurement system. The field dependence of the resistance was measured at several temperatures. Fields up to 8 T were employed. Figure 4.29 shows a typical set of results. A positive magnetoresistance over the entire range of magnetic field was observed in all diameter nanocylinders at all measured temperatures.

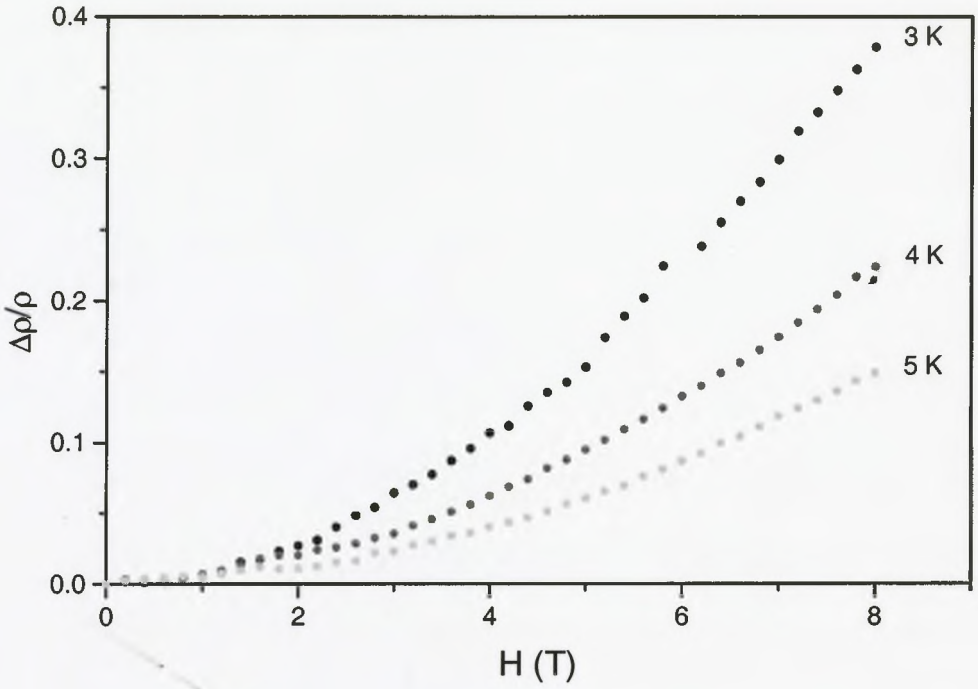

Figure 4.29 Dependence of $\Delta\rho/\rho$ on magnetic field H for a polypyrrole-filled 400 nm polycarbonate membrane, where ρ denotes the resistivity in the absence of an applied magnetic field and $\Delta\rho$ denotes the shift in resistivity resulting from the application of a magnetic field.

For variable range hopping conduction, a positive magnetoresistance is expected. According to theory, the field dependence of the resistivity is given by equation 2.8 with t = 5/2016 and y = 3/4 if the density of states is constant and with t = 0.0015 and y = 3/2 if the density of states is quadratic (section 2.2.3). The

former case corresponds to the Mott regime while the latter case corresponds to the Efros-Shklovskii regime, where Coulomb interactions are significant. In order to determine whether equation 2.8 was obeyed, the temperature dependence of the trans-membrane resistance was measured in the presence of a constant applied magnetic field. Fields of 2 T, and 5 T were used in separate trials. Plots of $\log\{\ln[\rho(H)/\rho(0)]\}$ against $\log T$ were used to derive the value of the exponent y. Figure 4.30 shows a typical $\log\{\ln[\rho(H)/\rho(0)]\}$ versus $\log T$ plot. For all diameter nanocylinders, a gradual change in slope was observed at 5 ± 1 K. The average value of y was 0.73 ± 0.30 for temperatures above about 5 K, and 1.63 ± 0.20 for temperatures below about 5 K. The former value overlaps 3/4 and the latter value overlaps 3/2. For the higher temperatures, plotting $\ln[\rho(H)/\rho(0)]$ against $T^{-3/4}$ yielded a straight line passing through the origin (Figure 4.31), in accordance with equation 2.8 with $y = 3/4$. For the lower temperatures, plotting $\ln[\rho(H)/\rho(0)]$ against $T^{-3/2}$ yielded a straight line passing through the origin (Figure 4.32), in accordance with equation 2.8 with $y = 3/2$. These results strongly suggest that the conduction mechanism above about 5 K was three dimensional Mott variable range hopping and that the conduction mechanism at lower temperatures was Efros-Shklovskii variable range hopping. This will be discussed in more detail at the end of the section.

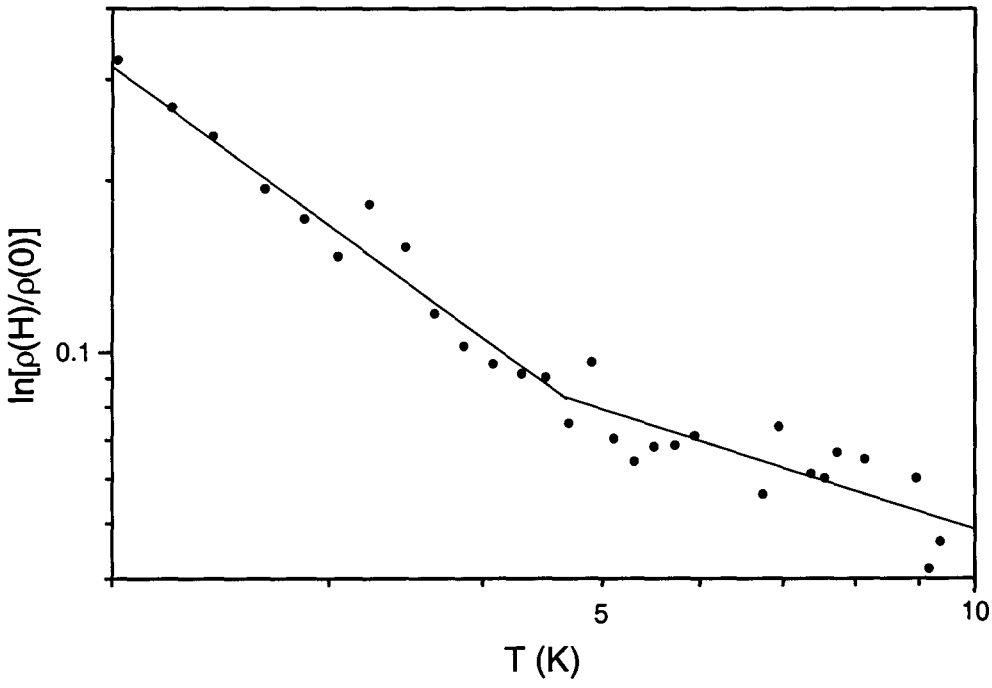

Figure 4.30 Log-log plot of {ln[ρ(H)/ρ(0)]} versus log *T* for a polypyrrole-filled 100 nm polycarbonate membrane with an applied field of 5 T. The solid lines are the lines of best fit over the temperature regions above and below 5 K.

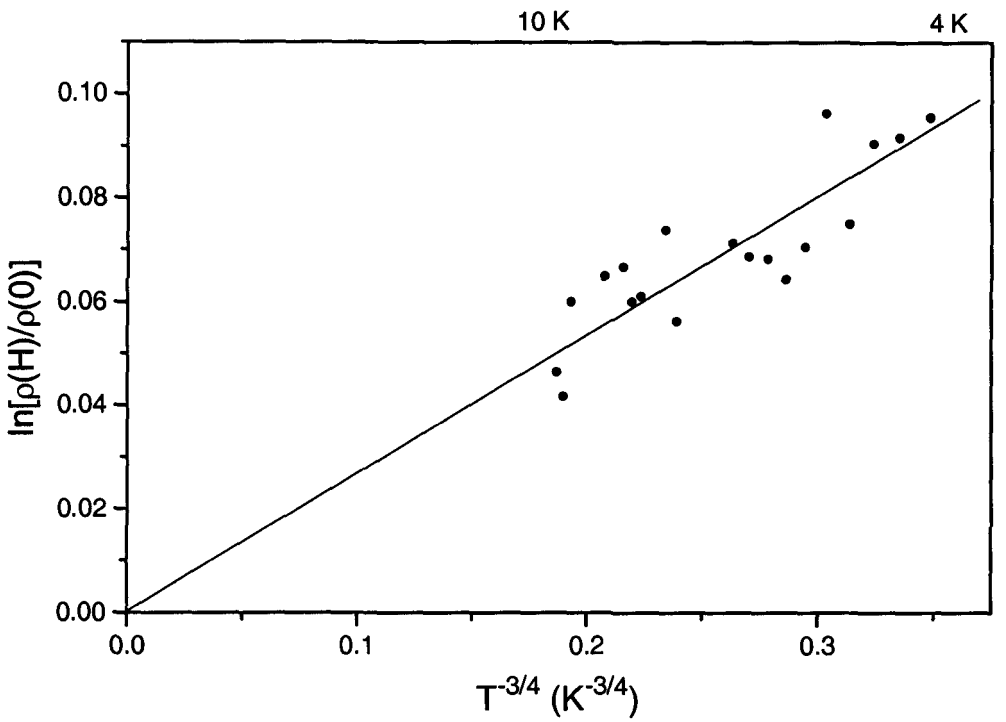

Figure 4.31 Plot of ln[ρ(H)/ρ(0)] versus $T^{-3/4}$ for a polypyrrole-filled 100 nm polycarbonate membrane with an applied field of 5 T.

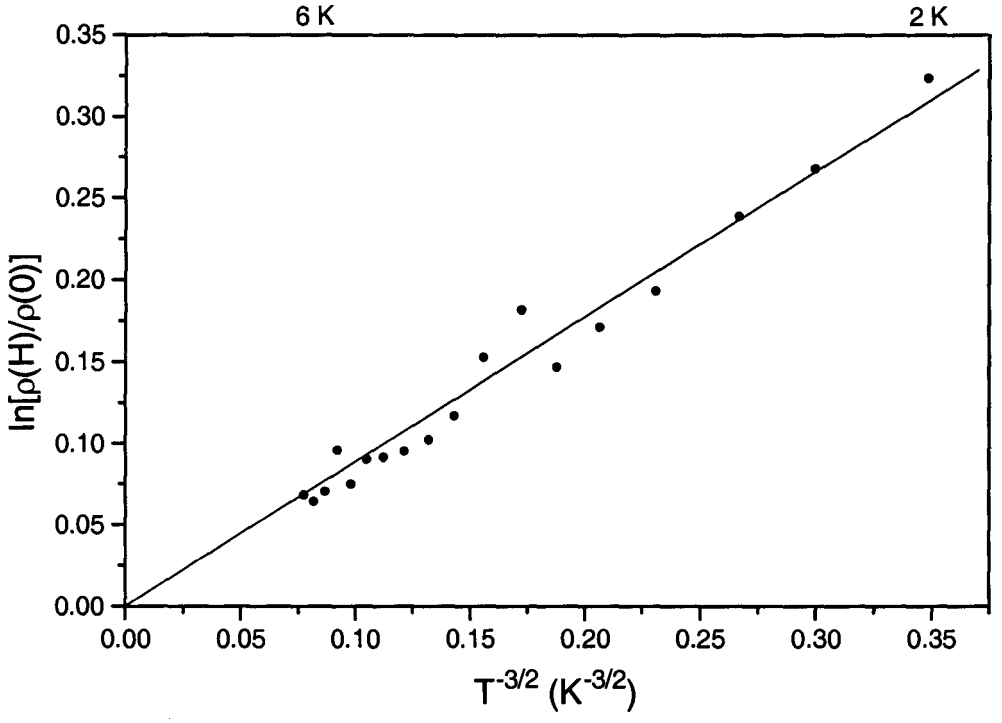

Figure 4.32 Plot of ln[ρ(H)/ρ(0)] versus $T^{-3/2}$ for a polypyrrole-filled 100 nm polycarbonate membrane with an applied field of 5 T.

In conjunction with the Mott characteristic temperatures T_0 obtained in section 4.2.1, the slopes of the ln[ρ(H)/ρ(0)] versus $T^{3/4}$ plots were used to calculate the charge carrier localization lengths L_{loc} for the various diameter nanocylinders. It was found that the localization length was 4.7 ± 0.4 nm for all diameter nanocylinders.

The localization length and the Mott characteristic temperatures were used in equation 2.4 (section 2.2.1) to calculate the temperature dependence of the average hopping distance R_{hop}. Because the uncertainty range associated with the R_{hop} values exceeded the range of variation between the R_{hop} values for the different diameter samples, a mean value was considered. Figure 4.33 shows a plot of R_{hop} versus $T^{-1/4}$. The average hopping distance increased from 5.8 ± 1.0 nm at 300 K to 16.2 ± 2.7 nm at 5 K.

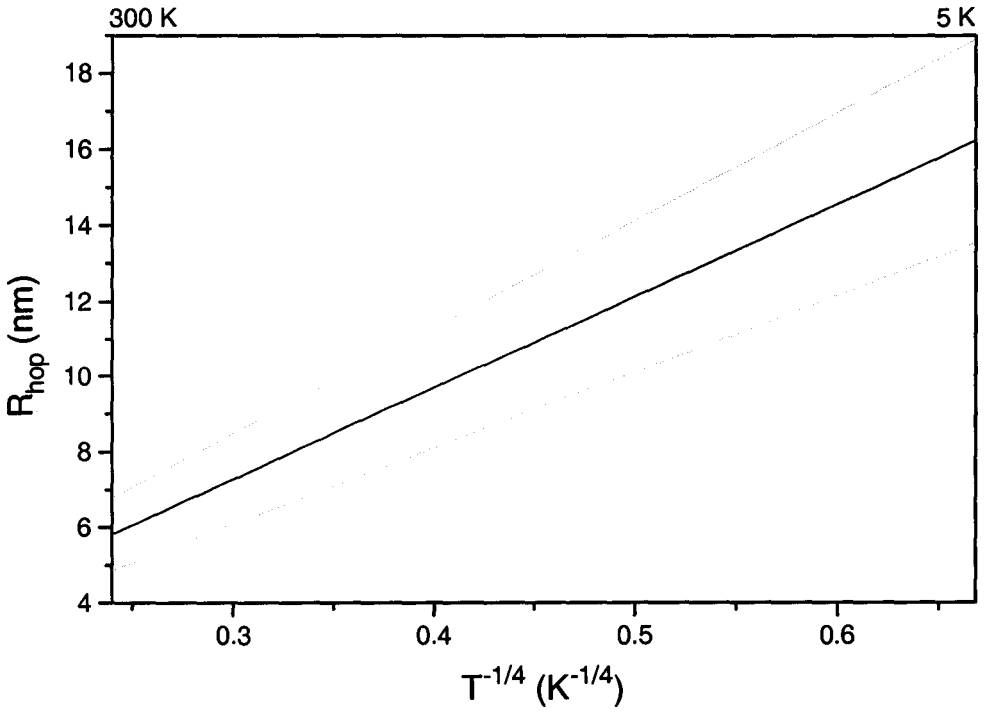

Figure 4.33 Average hopping distance R_{hop} versus $T^{-1/4}$. The gray lines delimit the uncertainty range.

Equation 2.3 (section 2.2.1) was used to calculate the density of states at the Fermi energy $N(E_F)$ in the Mott regime. The value of C_1 was taken to be 2. Figure 4.34 shows $N(E_F)$ plotted against nominal nanocylinder diameter. The density of states is slightly smaller for the smaller nanocylinder diameters. This is consistent with the observation that the smaller diameter nanocylinders were somewhat less conductive than the larger diameter nanocylinders.

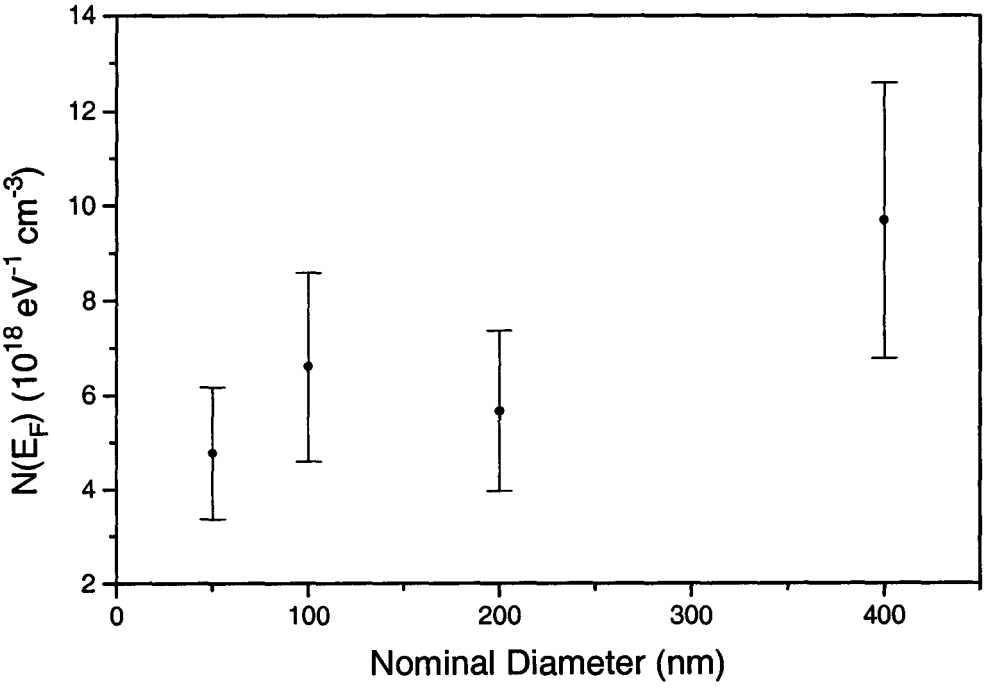

Figure 4.34 Density of states at the Fermi energy $N(E_F)$ versus nominal nanocylinder diameter.

There are no published accounts of magnetoresistance in polypyrrole nanocylinders with which to compare the above results. Nevertheless, the observed behavior is much like that seen in bulk samples of conducting polymers. The measured localization length of 4.7 ± 0.4 nm is similar to the 4.8 nm and 5.6 nm localization lengths measured by Ghosh *et al.* for polyaniline samples (Ghosh *et al.*, 1998). Furthermore, Ghosh *et al.* found that the average hopping distances for their samples was 10.6 nm and 11.5 nm at 50 K. This is comparable to the value of 9.1 ± 1.5 nm measured in the present study. The measured density of states values are within an order of magnitude of those reported by Meikap *et al.* (Meikap *et al.*, 1993) for polypyrrole and Ghosh *et al.* (Ghosh *et al.*, 1998) for polyaniline.

The observation of a crossover from Mott to Efros-Shklovskii variable range hopping at 5 ± 1 K is consistent with measurements on bulk polypyrrole by Meikap *et al.* (Meikap *et al.*, 1993). The possibility that the low temperature transition is indicative of one-dimensional Mott variable range hopping conduction (or some other form of one-dimensional hopping conduction) can be ruled out based on the following argument. In order for a transition from three dimensional to one-dimensional hopping to occur, the nanocylinder diameter or tube wall thickness must be comparable to the average hopping distance. At the observed transition temperature of about 5 K, the average hopping distance was found to be 16.2 ± 2.7 nm. This is much smaller in size than any of the nanocylinder

dimensions; especially for the 200 nm and 400 nm nanocylinders. Moreover, in variable range hopping, the average hopping distance increases with decreasing temperature. Hence, it is expected that if a three- to one-dimensional crossover were to occur in the nanocylinders, it would occur at a higher temperature for the smaller diameters. However, this was not observed: the transition temperature was 5 ± 1 K in all samples.

CHAPTER 5

CONCLUSION

Polypyrrole nanocylinders were successfully template synthesized within the pores of polycarbonate track-etched membranes and alumina membranes. Apparatus involving a horizontally-sitting membrane between vertically stacked pyrrole and iron chloride compartments was found to be superior to a side-by-side arrangement of compartments for producing uniformly filled template membranes.

An investigation of the effect of reaction time on the morphology of 50 nm polycarbonate membrane-templated nanocylinders showed that the polymer growth nucleated along the pore walls and subsequently grew radially inwards. After a sufficiently long reaction time, complete pore filling was achieved. TEM and SEM measurements on 50 nm, 100 nm, 200 nm, and 400 nm polycarbonate membrane-templated nanocylinders revealed a cigar-like shape. The tapering at the ends of the nanostructures was more pronounced in the smaller diameter nanocylinders. The alumina membrane-templated nanostructures were a linear chain of irregularly shaped blobs.

The electrical resistance and magnetoresistance of the polycarbonate-membrane templated samples was measured down to 1.8 K. Above 5 ± 1 K, three-dimensional Mott variable range hopping behavior was exhibited. Below 5 ± 1 K, a crossover to Efros-Shklovskii variable range hopping was observed. Based on the resistance and magnetoresistance results in the Mott regime, the localization length was found to be 4.7 ± 0.4 nm for all diameter nanocylinders. The average hopping distance in the Mott regime ranged from 5.8 ± 1.0 nm at 300 K to 16.2 ± 2.7 nm at 5 K. These quantities are far smaller than the nanocylinder dimensions; hence, no size effects, such as a crossover from three- to one-dimensional hopping, were observed.

Contrary to previous reports, the conductivity of the smaller diameter polycarbonate membrane-templated nanocylinders was slightly lower than that of the larger diameter nanocylinders. This result was supported by measurements of the Mott characteristic temperature T_0, which had a larger value for the smaller diameter nanocylinders, and by measurements of the density of states at the Fermi energy, which was smaller for the smaller diameter nanocylinders. It is expected that the disparity between the results of the present work and those of previous studies is primarily a consequence of differences in how the morphology of the nanocylinders was taken into account in calculating the conductivities. It was shown in the present study that if the cigar-like shape of the nanocylinders is

not taken into consideration, and the nanocylinders are treated as solid fibrils with the diameters given by the nominal pore diameters, then the calculated conductivity is aberrantly high for the smaller diameters.

The temperature dependence of the resistance across a polypyrrole-filled 100 nm alumina membrane was measured between room temperature and 78 K. Three-dimensional Mott variable range hopping behavior was observed. The value of the Mott characteristic temperature T_0 was the same size as that for similar diameter polycarbonate membrane-templated nanocylinders. This suggests that the conductivity of the two types of nanostructures was the same, despite the disordered structure of the alumina membrane-templated samples. Thus, it can be concluded that there is no conductivity-enhancing order in the polycarbonate membrane-templated nanocylinders.

BIBLIOGRAPHY

Abou-Elazab, T. F., Migahed, M. D., Park, H., Park, Y. W., MacNeillis, P., Rabenau, T., and Roth, S. (1996). *Synth. Met.* **76**, 281.

Bottger, H. and Bryksin, V. V. (1985). *Hopping conduction in solids.* VCH, Weinheim.

Bredas, J.L. and Street, G.B. (1985). *Acc. Chem. Res.* **18**, 309.

Cai, Z. and Martin, C. R. (1989). *J. Am. Chem. Soc.* **111**, 4139.

Cai, Z., Lei, J., Liang, W., Menon, V., and Martin, C. R. (1991). *Chem. Mater.* **3**, 960.

Chen, X., Devaux, J., Issi, J-P., and Billaud, D. (1995). *Polymer Engineering and Science* **35**, 642.

Conwell, E. M. (1997). *Handbook of organic conductive molecules and polymers:* Vol. 4. (ed. H. S. Nalwa), p. 1., John Wiley and Sons, New York.

Demoustier-Champagne, S. and Stavaux, P.Y. (1999). *Chem. Mater.* **11**, 829.

Duchet, J., Legras, R., and Demoustier-Champagne, S. (1998). *Synth. Met.* **98**, 113.

Epstein, A. J., Rommelmann, H., Bigelow, R., Gibson, H. W., Hoffmann, D. M., and Tanner, D. B. (1983). *Phys. Rev. Lett.* **50**, 1866.

Ghosh, M., Barman, A., De, S. K., and Chatterjee, S. (1998). *Synth. Met.* **97**, 23.

Hagiwara, T., Hirasaka, M., Sato, K., and Yamaura, M. (1990). Synth. Met. **36**, 241.

Hauser, J. J. (1976). *J. Non-Cryst. Solids* **23**, 21.

Hill, R. M. (1976). *Phys. Status Solidi A* **35**, K29.

Hjertberg, T., Norden, B., and Krutmeijer, E. (2001). 2000 Nobel poster for chemistry. Retrieved May 18, 2001, from http://www.nobel.se/chemistry /laureates/2000/illpres/index.html

Itaya, K., Sugawara, S., Kunio, A, and Saito, S. (1984). *Journal of Chemical Engineering of Japan* **17**, 514.

Knotek, M. L., Pollak, M., Donovan, T. M., and Kurtzman, H. (1973). *Phys. Rev. Lett.* **30**, 853.

Knotek, M. L. (1975). *Solid State Commun.* **17**, 1431.

Lorenz, B., Spatz, J. P., Hochheimer, H. D., Menon, V., Parthasarathy, R., Martin, C. R., Bechtold, J., and Hor, P. (1995). *Phil. Mag. B* **71**, 929.

Maddison, D. S. and Tansley, T. L. (1992). *J. Appl. Phys.* **72**, 4677.

Mansouri, J. and Burford, R. P. (1994). *Journal of Materials Science.* **29**, 2500.

Martin, C. R., Van Dyke, L. S., Cai, Z., and Liang, W. (1990). *J. Am. Chem. Soc.* **112**, 8977.

Martin, C. R. (1994). *Science* **266**, 1961.

Martin, C. R. (1995). *Acc. Chem. Res.* **28**, 61.

Meikap, A. K., Das, A., Chatterjee, S., Digar, M., and Bhattacharyya, S. N. (1993). *Phys. Rev. B.* **47**, 1340.

Menon, V. P., Lei, J., and Martin, C. R. (1996). *Chem. Mater.* **8**, 2382.

Mikat, J., Orgzall, I., Lorentz, B., Sapp, S., Martin, C. R., Burris, J. L., and Hochheimer H. D. (1999). *Physica B* **265**, 154.

Miller, A. and Abrahams, E. (1960). *Phys. Rev.* **120**, 745.

Mott, N. F. and Davis, E. A. (1979). *Electronic processes in non-crystalline materials.* Clarendon Press, Oxford.

Orgzall, I., Lorenz, B., Ting, S. T., Hor, P., Menon, V., Martin, C. R., and Hochheimer, H. D. (1996). *Phys. Rev. B* **54**, 16654.

Parthasarathy, R. and Martin, C. R. (1994). *Nature* **369**, 298.

Piraux, L., Dubois, S., Duvail, J. L., Radulescu, A., Demoustier- Champagne, S., Ferain, E., and Legras, R. (1999). *J. Mater. Res.* **14**, 3042.

Pollak, M., Knotek, M. L., Kurtzman, H., and Glick, H. (1973). *Phys. Rev. Lett.* **30**, 856.

Roth, S. and Bleier, H. (1987). *Adv. in Phys.* **36**, 385.

Roth, S. (1991). *Hopping transport in solids* (ed. M. Pollak and B. Shklovkii), p. 377. North Holland, Amsterdam.

Roth, S. (1995). *One-dimensional metals.* VCH, Weinheim.

Shante, V. K. S. and Varma, C. M. (1973). *Phys. Rev. B* **8**, 4885.

Shingubara, S., Okino, O., Sayama, Y., Sakaue, H., and Takahagi, T. (1997). *Jpn. J. Appl. Phys.* **36**, 7791.

Shklovskii, B.I. and Efros, A. L. (1984). *Electronic properties of doped semiconductors.* Springer-Verlag, Berlin.

Spatz, J. P., Lorenz, B., Weishaupt, K., Hochheimer, H. D., Menon, V., Parthasarathy, R., Martin, C. R., Bechtold, J., and Hor, P. (1994). *Phys. Rev. B.* **50**, 14888.

Tian, B., Zerbi, G. J. (1990). *J. Chem. Phys.* **92**, 3892.

Zabrodskii, A. G. and Zinov'eva, K. N. (1984). *Sov. Phys. JETP* **59**, 425.

Zhang, Y., Dai, P., Levy, M., and Sarachil, M. P. (1990). *Phys. Rev. Lett.* **64**, 2687.

APPENDIX

A.1 Calculation of Average Nanocylinder Length

Consider a pore which runs at an angle θ with respect to a membrane surface's normal, as depicted in Figure A.1. The length of the pore is L, and the thickness of the membrane is x. The length can be written as

$$L = \frac{x}{\cos\theta}. \tag{A.1}$$

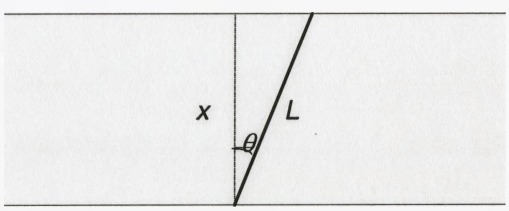

Figure A.1 Illustration of a portion of a membrane with a pore running at an angle θ with respect to the membrane surface's normal.

According to Demoustier-Champagne and Stavaux, the angle θ lies in the range $-34^\circ < \theta < +34^\circ$ (Demoustier-Champagne and Stavaux, 1999). If it is assumed that the pores are equally likely to be at any of the angles within the above range, then the average pore length is given by the average value of equation A.1 over $-34^\circ < \theta < +34^\circ$:

$$L_{avg} = \frac{\int_{(-34\pi/180)}^{(34\pi/180)} \frac{x\,d\theta}{\cos\theta}}{(34\pi/180) - (-34\pi/180)} \qquad \text{(A.2)}$$

$$= \left(\frac{17\pi x}{45}\right)\left[\ln\left(\frac{1+\sin\theta}{\cos\theta}\right)\right]_{\theta=(-34\pi/180)}^{\theta=(34\pi/180)}.$$

For membranes with a thickness of x = 10 μm, L_{avg} = 10.6 μm. For membranes with a thickness of x = 6 μm, L_{avg} = 6.4 μm.

A.2 Resistivity Across an Array of Parallel Model Nanocylinders

First, it is necessary to calculate the electrical resistance of a truncated cone. Consider a truncated cone with a large end radius r_o, a small end radius r_e, and a length ℓ. A cross-sectional view is shown in Figure A.2. The radius r can be written as a function of length y:

$$r(y) = \left(\frac{r_e - r_o}{\ell}\right) y + r_o. \tag{A.3}$$

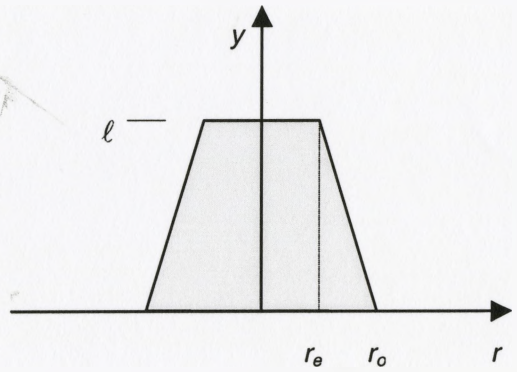

Figure A.2 Illustration of a truncated cone's cross section.

The truncated cone can be divided into a stack of infinitesimally thin disks of thickness dy. The contribution to the resistance from one such disk is

$$dR = \frac{\rho dy}{\pi r^2} \tag{A.4}$$

$$= \frac{\rho dy}{\pi\left[\left(\frac{r_e - r_o}{\ell}\right)y + r_o\right]^2}$$

where ρ is the resistivity. Integrating from $y = 0$ to $y = \ell$ yields the resistance of a truncated cone:

$$R_{tr.cone} = \int_0^{\ell} \frac{\rho dy}{\pi\left[\left(\frac{r_e - r_o}{\ell}\right)y + r_o\right]^2} \tag{A.5}$$

$$= \left(\frac{\rho\ell}{\pi(r_e - r_o)}\right)\left(\frac{-1}{\left[\left(\frac{r_e - r_o}{\ell}\right)y + r_o\right]}\right)_{y=0}^{y=\ell}$$

$$= \frac{\rho\ell}{\pi r_e r_o}.$$

The model nanocylinder consists of two truncated cones connected in series with a tubule[1]. The resistance of a hollow cylindrical tubule is

$$R_{tubule} = \frac{\rho L}{\pi\left(r_o^2 - r_i^2\right)}, \tag{A.6}$$

where r_i is the inner tubule radius and L is the tubule length. Thus, the resistance of a model nanocylinder is

$$R_{nanocyl.} = 2R_{tr.cone} + R_{tubule} \tag{A.7}$$

$$= \frac{\rho}{\pi}\left[\frac{2\ell}{r_e r_o} + \frac{L}{\left(r_o^2 - r_i^2\right)}\right].$$

For an electrically contacted membrane with a pore density of n and a contact area A, the number of contacted parallel nanocylinders is nA and the resistance R across the membrane is given by

$$\frac{1}{R} = \frac{nA}{R_{nanocyl.}} \quad . \tag{A.8}$$

[1] The 50 nm nanocylinders were solid; however, a solid fibril can be treated as a special case of a hollow tubule where the radius of the hollow is zero.

Hence,

$$R = \frac{R_{nanocyl.}}{nA} \tag{A.9}$$

$$= \frac{\rho}{\pi n A}\left[\frac{2\ell}{r_e r_o} + \frac{L}{\left(r_o^2 - r_i^2\right)}\right].$$

Therefore, the resistivity of the array of parallel model nanocylinders is

$$\rho = \pi n A R\left[\frac{2\ell}{r_e r_o} + \frac{L}{\left(r_o^2 - r_i^2\right)}\right]^{-1}. \tag{A.10}$$